



# Numerical simulations and modelling of mass transfer through random assemblies of catalyst particles: from dilute to dense reactive particulate regime

Mostafa Sulaiman, Eric Climent, Anthony Wachs, Abdelkader Hammouti

## ► To cite this version:

Mostafa Sulaiman, Eric Climent, Anthony Wachs, Abdelkader Hammouti. Numerical simulations and modelling of mass transfer through random assemblies of catalyst particles: from dilute to dense reactive particulate regime. Chemical Engineering Science, 2020, 223, pp.115659. 10.1016/j.ces.2020.115659 . hal-02940301

**HAL Id: hal-02940301**

**<https://ifp.hal.science/hal-02940301>**

Submitted on 30 Apr 2021

**HAL** is a multi-disciplinary open access archive for the deposit and dissemination of scientific research documents, whether they are published or not. The documents may come from teaching and research institutions in France or abroad, or from public or private research centers.

L'archive ouverte pluridisciplinaire **HAL**, est destinée au dépôt et à la diffusion de documents scientifiques de niveau recherche, publiés ou non, émanant des établissements d'enseignement et de recherche français ou étrangers, des laboratoires publics ou privés.



## Open Archive Toulouse Archive Ouverte



OATAO is an open access repository that collects the work of Toulouse researchers and makes it freely available over the web where possible

This is an author's version published in: <https://oatao.univ-toulouse.fr/27535>

### Official URL:

<https://doi.org/10.1016/j.ces.2020.115659>

### To cite this version:

Sulaiman, Mostafa  and Climent, Éric  and Wachs, Anthony and Hammouti, Abdelkader *Numerical simulations and modelling of mass transfer through random assemblies of catalyst particles: from dilute to dense reactive particulate regime.* (2020) Chemical Engineering Science, 223. 115659. ISSN 0009-2509

Any correspondence concerning this service should be sent  
to the repository administrator: [tech-oatao@listes-diff.inp-toulouse.fr](mailto:tech-oatao@listes-diff.inp-toulouse.fr)

# Numerical simulations and modelling of mass transfer through random assemblies of catalyst particles: From dilute to dense reactive particulate regime

Mostafa Sulaiman <sup>a,c</sup>, Eric Climent <sup>c,\*</sup>, Anthony Wachs <sup>d,e</sup>, Abdelkader Hammouti <sup>a,b</sup>

<sup>a</sup> IFP Énergies Nouvelles, Fluid Mechanics Department, Rond-point de l'échangeur de Solaize, BP 3, 69360 Solaize, France

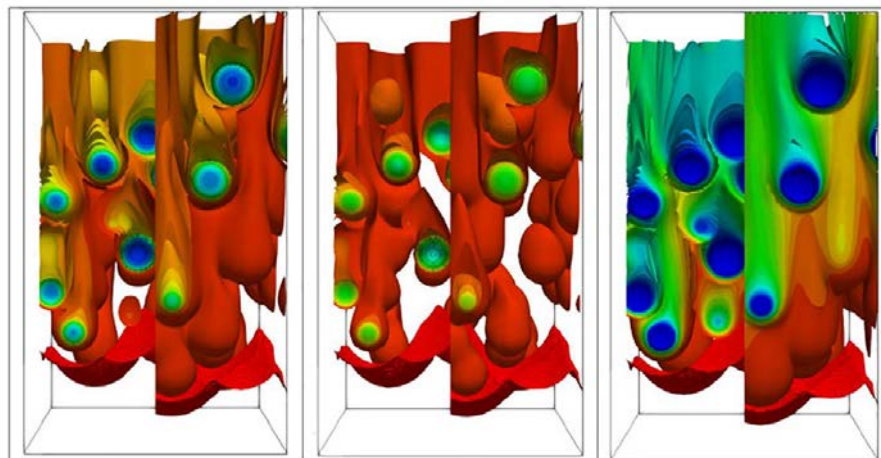
<sup>b</sup> INRS-ETE, Université du Québec, 490, Rue de la Couronne, Québec G1K 9A9, Canada

<sup>c</sup> Institut de Mécanique des Fluides de Toulouse (IMFT), Université de Toulouse, CNRS, Toulouse, France

<sup>d</sup> Department of Mathematics, University of British Columbia, 1984 Mathematics Road, Vancouver, BC V6T 1Z2, Canada

<sup>e</sup> Department of Chemical and Biological Engineering, University of British Columbia, 2360 East Mall, Vancouver, BC V6T 1Z3, Canada

## GRAPHICAL ABSTRACT



## ABSTRACT

We study mass transfer through random assemblies of fixed spherical catalyst particles experiencing an external convective diffusive fluid stream. Chemical species are transported through the array and are diffused from fluid to solid phase through particles surface. An internal first order irreversible chemical reaction takes place within the porous catalyst particles. We address the determination of mass transfer coefficient by performing direct numerical simulations with fully internal external coupling using concentration and flux continuity boundary conditions at the solid fluid interface. We derive a theoretical prediction of the profiles of cup mixing concentration, average of mean surface and average of mean volume concentration of the particles along the height of the domain. The model for the dimensionless mass transfer coefficient ('reactive' Sherwood number) is accounting for the five dimensionless parameters that control the physics of the system: the Reynolds number  $Re$ , the Schmidt number  $Sc$ , the Damköhler number  $Da$ , the internal to external diffusion coefficient ratio  $\gamma$  and the solid volume fraction  $\alpha_s$ . We use a coupled Sharp Interface/ Discrete Lagrange Multiplier Fictitious Domain Method (SIM DLM/ FD), thoroughly validated in our previous study (Sulaiman et al., 2019) to test the accuracy of the model

### Keywords:

Porous catalyst particles  
Chemical reaction  
Mass transfer  
Direct numerical simulations  
Sherwood number

\* Corresponding author.

E-mail address: [eric.climent@imft.fr](mailto:eric.climent@imft.fr) (E. Climent).

over a wide range of dimensionless parameters and solid volume fraction (from dilute  $\alpha_s = 0.1$  to dense regime  $\alpha_s = 0.5$ ). We show and discuss the limitations of the proposed model.

## 1. Introduction

Chemical reactors composed of solid particles dispersed in a fluid phase are commonly operated in many industrial facilities. In petrochemical processes, catalytic fixed bed reactors (Wehinger et al., 2015) and catalytic fluidized bed reactors (Gao et al., 2008) are widely operated in refineries for cracking long chain hydrocarbons into lighter products. Biomass catalytic co pyrolysis processes (Zhang et al., 2018), biomass gasification (Bridgwater, 1995; Turn et al., 1998) and biomass complete combustion (Baxter, 1993) are processes involving multiphase flows with chemical reactions in particles. In such systems, many transport phenomena take place, such as heat, mass, and momentum transfer. The performance prediction, design, and optimization of these reactors necessitate a better comprehension of the coupling among the various occurring physical and chemical phenomena taking place in there.

Particle Resolved Direct Numerical Simulations (PR DNS or PRS) that fully resolve local interactions between the two phases is an emerging approach to understand the coupling between transport phenomena and chemical reactions. Indeed, high performance computing with increasing CPU efficiency has encouraged scientists to develop numerical methods to solve momentum and mass balance equations on grids finer than the particle size. PRS is able, so far, to simulate particulate flow systems consisting of thousands of particles and provide reliable information about local interactions at the particle scale (Sun et al., 2016). However, DNS is unable to simulate industrial scale systems that contain billions of particles. The local interactions resolved by DNS at the particle scale can be modeled by correlations or closure laws, such as a drag coefficient correlation for momentum transfer (Deen et al., 2014), a Nusselt number correlation for heat transfer and a Sherwood number correlation for mass transfer. In fluidized beds or turbulent flows seeded with particles, the solid volume fraction varies over a wide range from dilute to dense regions due to preferential accumulation and the formation of clusters. These closure laws can be used in a multi scale analysis (van der Hoef et al., 2004) to enhance the accuracy of numerical methods such as CFD DEM, that are able to simulate systems with large number of particles but do not resolve the flow and transfers below the particle scale.

Many PRS methods are available in literature to simulate particulate flow problems. The methods with a fixed Cartesian mesh have the advantage of very good scalability on supercomputers. Their disadvantage lies in the difficulty of imposing accurately the correct boundary conditions on the surface of each particle. The Immersed Boundary Method (IBM) (Uhlmann, 2005), is a fixed mesh computational method, that imposes boundary conditions at the particle surface by means of Lagrangian markers. Both the smooth version of (Uhlmann, 2005) and a high order ghost cell version have been applied by Xia et al. (2014) to study convective heat/mass transfer for a single particle. IBM was also used to evaluate the heat transfer Nusselt number in dense particulate flow systems by Deen et al. (2014) and Sun et al. (2015). More recently, Lu et al. (2018) employed an IBM to study mass transfer with a first order irreversible surface chemical reaction. (Derksen, 2014) coupled IBM with the Lattice Boltzmann Method (LBM) to study mass transfer through fixed and fluidized beds of particles. (Bohn et al., 2012) studied gas solid diffusion reaction within a single particle. The Distributed Lagrange Multiplier/ Fictitious Domain Method

(DLM/FD) is an alternative approach. Firstly introduced by Glowinski et al. (2001), and it combines the particle and fluid balance equations into a general weak formulation on a fixed Cartesian mesh. The DLM/FD method has been used to simulate heat/mass transfer by Yu et al. (2006), Dan and Wachs (2010) and Wachs (2011).

In addition, the Sharp Interface Method (SIM), or as alternatively referred to, the Ghost Fluid Method (GFM), is a fixed mesh computational method that accurately enforces boundary conditions with discontinuities along embedded interfaces (Shi et al., 2011). Jump conditions are incorporated into the discretization of the differential operators on a Cartesian grid in the vicinity of the interface. The SIM was firstly introduced by Fedkiw et al. (1999). Shao et al. (2012) combined the SIM with a fictitious domain method to simulate heat transfer inside and outside particles. More recently, Sulaiman et al. (2019b) coupled the SIM to a fictitious domain method to study mass transfer for three interacting aligned catalyst particles undergoing a first order irreversible chemical reaction.

In this work, we study the effect of a first order irreversible chemical reaction on mass transfer in a random assembly of fixed particles. The reaction takes place within the catalyst particles composing the assembly. The fluid enters the system with an imposed inlet concentration and transports chemical species through the particle array. For infinite reaction rate, the system is analogous to heat transfer problems (Sun et al., 2016; Deen et al., 2014; Tavassoli et al., 2013 and Gunn, 1978) for which temperature is imposed at the particle surface. The analogy with heat transfer fails when the reaction rate is finite. According to the reaction kinetics, one of the three following regimes can predominate. (i) When the reaction rate is very slow compared to diffusion, the surface concentration of the particles is equal to the bulk concentration in the fluid and the regime is chemically controlled. (ii) When the reaction rate is infinitely fast compared to diffusion, the surface concentration approaches zero and the system is controlled by mass transfer (diffusion limited), (iii) In between the two previous cases, the system is neither mass transfer controlled nor kinetics controlled, and the catalyst surface concentration is a priori unknown. In our previous work (Sulaiman et al., 2019a) and Sulaiman et al. (2019b), for a single particle and three interacting particles, respectively, we presented models for the 'reactive' Sherwood number that accounts for the effect of an internal chemical reaction and diffusion in the solid phase coupled to external convection and diffusion in the fluid phase.

Our objective in the present work is to extend our model to account for the effect of the solid volume fraction on the reactive Sherwood number in the flow through a random array of fixed reactive particles. We do not consider the specific case of closely packed bed reactors but address more generally the effect of solid volume fraction on mass transfer as would be the case of solid particles suspended in a fluid flow. The paper is organized as follows. First, we introduce the balance equations and the numerical method is briefly described referencing former papers on benchmarks and validations. We describe also the numerical setup for the simulation in a random assembly of particles. In the third section, we present the theoretical modeling of mass transfer coupled to chemical reaction which has been extended in the present paper to account for the effect of solid volume fraction. Finally numerical simulation results are compared to the theoretical prediction and

conclusions are drawn on the range of validity and limitations of the present approach.

## 2. Balance equations and numerical setup

### 2.1. Governing equations

We solve the time dependent and incompressible flow of a Newtonian fluid around multiple fixed solid particles with mass transfer from the fluid to particles. Chemical reaction occurs within the solid catalytic porous particles without considering heat transfer. Only diffusion is considered inside the particles because we assume permeability to be low. We define the full flow domain as  $\Omega$ , the part of  $\Omega$  occupied by the solid particles as  $P$  and the part of  $\Omega$  occupied by the fluid as  $\Omega \setminus P$ . The problem is governed by the fluid mass conservation equation, fluid momentum balance and chemical species transport and reaction equations. The fluid density and viscosity are considered to be constant by assuming a single solute under low concentration  $C$  in the fluid. Dimensional quantities are distinguished from dimensionless quantities by a <sup>\*</sup> superscript. We denote  $\mathbf{u}^*$  the fluid velocity,  $p^*$  the fluid pressure,  $C_f^*$  the chemical species concentration in the fluid and  $C_s^*$  the chemical species concentration in the particles. The chemical species is undergoing a first order irreversible reaction in the solid particles. With appropriate initial conditions in  $\Omega$  on  $(\mathbf{u}^*, C_f^*, C_s^*)$  and boundary conditions on  $\partial\Omega$ , the boundary of  $\Omega$ , on  $\mathbf{u}^*$  (and potentially on  $p^*$ ), the set of conservation equations together with fluid/solid interface conditions is written as follows:

- in the fluid

$$\rho_f^* \left( \frac{\partial \mathbf{u}^*}{\partial t^*} + (\mathbf{u}^* \cdot \nabla) \mathbf{u}^* \right) - \eta^* \nabla^2 \mathbf{u}^* + \nabla p^* = \mathbf{0}, \quad (1)$$

$$\nabla \cdot \mathbf{u}^* = 0, \quad (2)$$

$$\frac{\partial C_f^*}{\partial t^*} + \mathbf{u}^* \cdot \nabla C_f^* - \nabla \cdot (D_f^* \nabla C_f^*) = 0, \quad (3)$$

where  $\rho_f^*$  denotes the fluid density,  $\eta^*$  the fluid viscosity and  $D_f^*$  the chemical species diffusion coefficient in the fluid.

- in the solid

$$\mathbf{u}^* = \mathbf{0}, \quad (4)$$

$$\frac{\partial C_s^*}{\partial t^*} - \nabla \cdot (D_s^* \nabla C_s^*) - k_s^* C_s^* = 0, \quad (5)$$

where  $D_s^*$  denotes chemical species effective diffusion coefficient and  $k_s^*$  the effective first order reaction constant in the solid. The molecular diffusion and reaction constant of the kinetics are related to the internal micro structure of the porous media (porosity, tortuosity and specific area for the catalytic reaction). We thus assume that they can be approximated by a continuous model in which the effective diffusion coefficient in solid phase is typically ten to hundred times lower than in fluid phase. Bruggeman's correlation states that tortuosity scales with porosity to the power  $-1/2$  yielding in our cases a porosity of catalytic particles varying from 0.04 and 0.2. Therefore, the flow cannot penetrate within particles of very low permeability and the reactive solute only diffuses inside the catalytic porous particles.

- at the fluid/solid interface  $\partial P$

$$\mathbf{u}^* = \mathbf{0}, \quad (6)$$

$$C_s^* = C_f^*, \quad (7)$$

$$D_s^* \frac{\partial C_s^*}{\partial \mathbf{n}} = D_f^* \frac{\partial C_f^*}{\partial \mathbf{n}}, \quad (8)$$

where  $\mathbf{n}$  denotes the unit vector normal to the fluid/solid interface. Balance equations are made dimensionless by introducing a characteristic length  $L_c^*$ , a characteristic velocity  $U_c^*$  and a characteristic convective time  $T_c^* = L_c^*/U_c^*$ . As solid particles are spheres, we choose  $L_c^*$  as particle diameter  $d_p^*$ . When the problem is not purely diffusive, an obvious choice for  $U_c^*$  is the far field inlet velocity  $U_{in}^*$ . Also, by normalizing the chemical species concentration between 0 and 1 and introducing the chemical species diffusion coefficient ratio  $\gamma = \frac{D_s^*}{D_f^*}$ , conservation Eqs. (3) and (5) together with boundary conditions (7) and (8), i.e., continuity of chemical species concentration and continuity of chemical species normal flux density, can be recast into a single dimensionless conservation equation for the chemical species  $C$  with appropriate continuity conditions at the fluid/solid interface on the chemical species concentration and on its normal flux. The set of dimensionless equations eventually reads as follows:

$$\frac{\partial \mathbf{u}}{\partial t} + (\mathbf{u} \cdot \nabla) \mathbf{u} - \frac{1}{Re} \nabla^2 \mathbf{u} + \nabla p = \mathbf{0} \quad \text{in } \Omega \setminus P, \quad (9)$$

$$\nabla \cdot \mathbf{u} = 0 \quad \text{in } \Omega \setminus P, \quad (10)$$

$$\mathbf{u} = \mathbf{0} \quad \text{in } P \cup \partial P, \quad (11)$$

$$\frac{\partial C}{\partial t} + \mathbf{u} \cdot \nabla C - \nabla \cdot \left( \frac{h(\gamma)}{Pe} \nabla C \right) + \frac{h(\gamma)g(\phi^2)}{Pe} C = 0 \quad \text{in } \Omega, [C]_{\partial P} = 0, \left[ h(\gamma) \frac{\partial C}{\partial \mathbf{n}} \right]_{\partial P} = 0, \quad (12)$$

where  $[\ ]_{\partial P}$  represents the jump condition across the fluid/solid interface. The dimensionless numbers introduced above are defined as follows:

- Reynolds number:  $Re = \frac{\rho_f^* U_{in}^* L_c^*}{\eta^*}$ , characterizes the external flow regime,
- Peclet number:  $Pe = \frac{U_{in}^* L_c^*}{D_f^*}$ , characterizes convective to diffusive external transport,
- Damköhler number:  $Da = \phi^2 \frac{k_s^* L_c^{*2}}{D_s^*}$ , characterizes reaction to diffusion rates where  $\phi = \sqrt{Da}$  is the Thiele modulus, and the functions  $h(\gamma)$  and  $g(\phi^2)$  are simple Heavyside like functions defined as:

$$h(\gamma) = \begin{cases} 1 & \text{in } \Omega \setminus P, \\ \gamma & \text{in } P. \end{cases}$$

$$g(\phi^2) = \begin{cases} 0 & \text{in } \Omega \setminus P, \\ \phi^2 & \text{in } P. \end{cases}$$

As usual, we can also introduce a Schmidt number  $Sc = \frac{\eta^*}{\rho_f^* D_f^*}$  such that  $Pe = Re \cdot Sc$ . Hence the external mass transfer is equivalently characterized by the pair  $(Re, Pe)$  or the pair  $(Re, Sc)$ .

The range of physical quantities are summarized in Table (1) referring to gas solid and liquid solid in industrial applications.

**Table 1**

Physical properties of industrial gas-solid and liquid-solid reactive particulate systems.

Parameter	Catalyst particle	Liquid	Gas
$D$ (m <sup>2</sup> s <sup>-1</sup> )	10 <sup>-6</sup> – 10 <sup>-10</sup>	~ 10 <sup>-9</sup>	10 <sup>-6</sup> – 10 <sup>-5</sup>
$r_p$ (mm)	1 – 5	–	–
$k_s$ (s <sup>-1</sup> )	10 <sup>-6</sup> – 10;	–	–
$U_c$ (cm s <sup>-1</sup> )	–	1–2	0.2–20
$\mu_f$ (mPa s)	–	0.386–0.92	~ 0.9
$\rho_f$ (kg m <sup>-3</sup> )	–	695–770	~ 100

Liquids are hydrocarbons such as Heptane, Decane, or Hexadecane. Gases are a mixture of hydrogen gas and hydrocarbons. According to this table the parameter ranges are:  $\gamma \in [0.01, 1]$ ,  $\phi \in [0.01, 3]$ ,  $Re \in [0, 200]$ , and  $Sc \in [1, 1000]$ .

## 2.2. Numerical model

We employ our previously validated Finite Volume/Staggered Grid DLM/FD solver implemented in our code PeliGRIFF. The whole method is fully detailed in Wachs et al. (2015), Rahmani and Wachs (2014) for freely moving particles and in Dorai et al. (2015) for fixed obstacles and was pioneered by Glowinski et al. (1999) in a Finite Element context. We solve the fluid conservation Eqs. (9) and (10) on a Cartesian structured mesh of uniform grid size everywhere in the domain (not only in  $\Omega \setminus P$  but in the entire  $\Omega$ ) and we enforce motionless obstacles (represented by (11)) in the region (filled with fictitious fluid) occupied by particles using a distributed Lagrange multiplier field. A collocation point method is used to discretize the solid obstacles on the fluid mesh and a second order interpolation of the fluid velocity at the particle boundary (Wachs et al., 2015; Rahmani and Wachs, 2014; Dorai et al., 2015). The strength of our method is that it does not require any kind of hydrodynamic radius calibration (see Wachs et al. (2015) for more details about hydrodynamic radius calibration). The spatial discretization of the diffusive operator in (13) on the non boundary fitted mesh is achieved by a Sharp Interface Method (Fedkiw et al., 1999; Liu et al., 2000; Shao et al., 2012) through which we account for the continuity of  $C$  and its normal flux across the fluid/solid interface through the two boundary conditions  $[C]_{\partial P} = 0$  and  $[h(\gamma) \frac{\partial C}{\partial n}]_{\partial P} = 0$ , respectively. The method is first order accurate in space and it incorporates the jump conditions into the spatial discretization of the diffusive term whereas the other terms in (13) are discretized in a classical way. For the complete implementation of the method in 3D and its validation the reader is referred to Sulaiman et al. (2019b). The overall spatial accuracy of the discretization scheme is however not fully 2<sup>nd</sup> order due to the non boundary fitted mesh around the solid obstacles. The dimensionless mesh size  $\Delta x$  is related to the number of points per particle diameter through  $N_p = 1/\Delta x$ .  $N_p$  can be related to numerical precision by referring to our previous convergence study presented in Sulaiman et al. (2019b). When only transfer is involved the value of  $N_p$  is typically 24 to achieve a precision of less than 5% error. To keep the same level of accuracy, the number of grid points per particle diameter is increased to 40 in the presence of chemical reaction which has the tendency to make the boundary layers thinner.

The chemical species problem is one way coupled to the fluid problem through the velocity field  $\mathbf{u}$ . The discretized conservation Eq. (12) reads as follows for 1<sup>st</sup> order scheme while the reactive term is treated implicitly:

$$\frac{C^{n+1} - C^n}{\Delta t} - \nabla \cdot \left( \frac{h(\gamma)}{Pe} \nabla C^{n+1} \right) + \frac{h(\gamma)g(\phi^2)}{Pe} C^{n+1} = \frac{1}{2} \left( 3\mathbf{u}^{n+1} \cdot \nabla C^n - \mathbf{u}^n \cdot \nabla C^{n-1} \right) \quad (13)$$

We solve the full problem as a sequence of a non stationary fluid problem for a given  $Re$  until the steady state is reached for the Reynolds numbers we considered. We then follow the fluid problem by a chemical species problem for a given  $[Da, Sc]$  using the computed velocity field until temporal convergence. (see Fig. 1)

## 2.3. Description of geometry and particles spatial distribution

We consider the simulation domain in Fig. 2 which is uniformly discretized on Cartesian grid. The domain dimensions are set to

$L_x = L_y$  and  $L_z$ , which are given in next sections. Particles are randomly distributed in the packing region  $x \in [0, L_x]$ ,  $y \in [0, L_y]$  and  $z \in [\Delta l, L_z - \Delta l]$ , where  $\Delta l$  is the inlet/outlet zone which is left free of particles. The fluid enters the domain from the bottom boundary with an imposed constant dimensionless velocity  $\mathbf{u} = (0, 0, 1)$  and an imposed concentration  $C_\infty = 1$ . Periodic boundary conditions are imposed in  $x$  and  $y$  directions while a classical outflow boundary condition  $\frac{\partial u}{\partial z} = \frac{\partial C}{\partial z} = 0$  and  $p = p_{ref} = 0$  is imposed at the outlet (top) boundary. In the configuration of packed beds, (Bale et al., 2017) used PRS to characterize the effect of walls that may confine the bed of particles on mass transfer coefficient for low Reynolds number. (Bale et al., 2018) also used PRS to study the inlet and end effects on mass transfer and drew the conclusion that homogeneity of transfer is achieved after two sphere diameters downstream from the bottom of the bed and effect starts from one sphere diameter upstream of the top of the bed. The solid phase consists of catalyst particles experiencing diffusion of the solute and chemical reaction. The solid volume fraction  $\alpha_s$  is chosen such that  $\alpha_s \in [0.1, 0.5]$  to derive a model which would be valid from the dilute to the dense regime. We consider three values for solid volume fraction;  $\alpha_s = 0.1$  (55 particles),  $\alpha_s = 0.3$  (165 particles) and  $\alpha_s = 0.5$  (275 particles), i.e., from a semi dilute regime to a rather dense regime. Up to  $\alpha_s = 0.3$ , particles are randomly distributed through a random seeding of non overlapping spheres. For  $\alpha_s = 0.5$ , particles are initially distributed at solid volume fraction  $\alpha_{si} = 0.25$ , with particles diameter  $d_{pi} < d_p$ . Then, the particles' radius is expanded. During expansion, particles experience multiple collisions before they reach the final diameter  $d_p$ , that satisfies the desired value of  $\alpha_s$ . We use five independent random particle configurations for each mass transfer simulation. According to the convergence study of Sun et al. (2016), this permits to reach a 95% statistical convergence on numerical results. This is consistent with the spatial resolution  $N_p$  we selected ensuring a maximum of 5% error.

## 3. Modeling of mass transfer through assembly of particles

The theoretical modeling is described in this section. First we compare our numerical simulation results to the literature for mass transfer in a random assembly of particles. Then, we consider chemical reaction and present the model for a single particle and extend it to account for solid volume fraction.

### 3.1. Non reactive mass transfer

The classical way of predicting mass transfer in a two phase fluid solid reactor (catalyst particles undergoing an internal diffusion reaction, associated to an external convection diffusion) is to decouple the internal and external transfer in the system. Then the two separated problems are coupled at the solid fluid interface, through concentration and flux continuities. Thus, based on the assumption of uniform external mass transfer coefficient, estimated from correlations on Sherwood number, and using the interface condition, the external and internal transport phenomena are coupled. As a first step, we evaluate the reference Sherwood number in mass transfer controlled regimes,  $Da \rightarrow \infty$ , i.e. an infinite reaction rate. The system in this case is analogous to heat transfer problem with particles at fixed temperature. We define the cup mixing, or flow averaged concentration as:

$$\bar{C}(z) = \frac{\int_{S_f} u_z(x, y, z) C(x, y, z) dx dy}{\int_{S_f} u_z(x, y, z) dx dy} \quad (14)$$

where  $S_f$  denotes the cross section area of the fluid and  $u_z$  denotes the fluid velocity component along the  $z$  direction. Assuming that

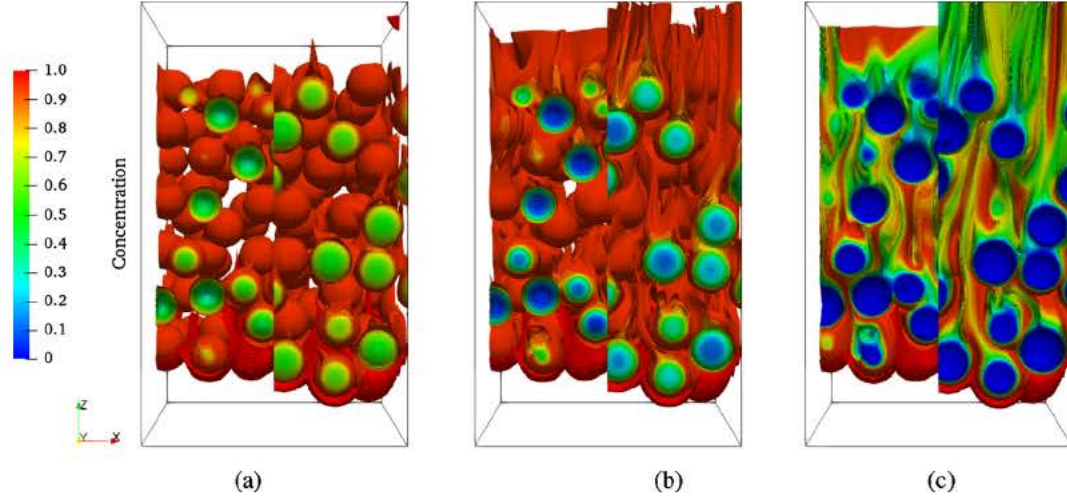


Fig. 1. Concentration isosurfaces for  $Re = 25, Sc = 1, \gamma = 0.1, \alpha_s = 0.3$  and different Damköhler numbers. (a)  $Da = 40$ , (b)  $Da = 200$  and (c)  $Da = \infty$ .

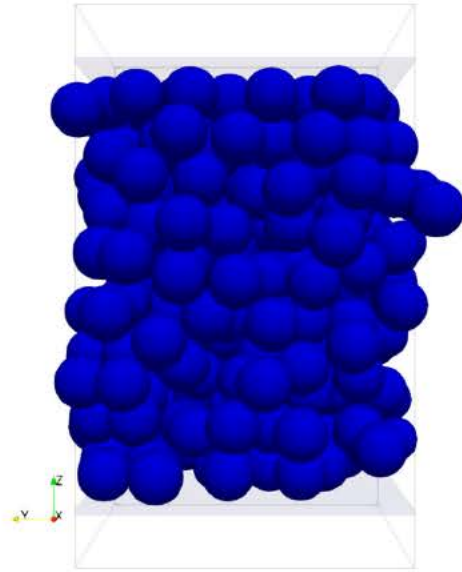


Fig. 2. Simulation domain with a random assembly of particles at  $\alpha_s = 0.5$ .

axial dispersion is negligible, the balance equation for the cup mixing averaged concentration in the system along the  $z$  direction is written as follows:

$$\frac{d\bar{C}(z)}{dz} + \xi(\bar{C}(z) - C_s) = 0 \quad (15)$$

where  $C_s$  is the particle concentration and  $\xi$  is characteristic of external mass transfer, defined as (16):

$$\xi = \frac{6\alpha_s Sh}{Pe} \quad (16)$$

Hence, the concentration profile along the  $z$  direction in the bed, i.e. the solution of (15), is written as:

$$\bar{C}(z) = (C_\infty - C_s) \exp(-\xi z) + C_s \quad (17)$$

In the above equation the value of  $\xi$  can be determined by fitting the concentration profile obtained numerically with the analytical solution (17).  $\alpha_s$  and  $Pe$  being fixed, the value of  $\xi$  obtained by the fitting yields the value of the Sherwood number corresponding to our numerical simulation results.

We perform a set of numerical simulations at constant  $Sc = 1$  and  $Re \in [0, 100]$ . We consider two solid volume fractions  $\alpha_s = 0.1$  and  $\alpha_s = 0.3$ . The particle surface concentration is fixed to zero by setting  $k'_s$  to a very high value that models  $Da = \infty$ . We calculate  $Sh$  by fitting numerical simulation results to the 1D model (17). For each  $(Re, Sc, \alpha_s)$  we take the average of  $Sh$  resulting from 5 different random particle assemblies. The numerical spatial resolution in this case is set to  $N_p = 24$  and simulations are performed at  $CFL < 0.25$  to reach temporal convergence. Domain dimensions are  $L_x = L_y = 6, L_z = 16$ , and  $\Delta t = 4$ . We compare the Sherwood number obtained from our simulations with the previously established correlations of (Sun et al., 2016; Deen et al., 2014 and Gunn, 1978) in Fig. 3. Our numerical simulation results show higher mass transfer estimate than those of (Deen et al., 2014 and Sun et al., 2016) correlations for  $\alpha_s = 0.1$  while a better agreement is observed for  $\alpha_s = 0.3$ . The numerical results at  $\alpha_s = 0.3$  are closer to both correlations than those at  $\alpha_s = 0.1$ . In both cases the results are below those of (Gunn, 1978) correlation (18), with  $\alpha_f = 1 - \alpha_s$  is the porosity of the bed.

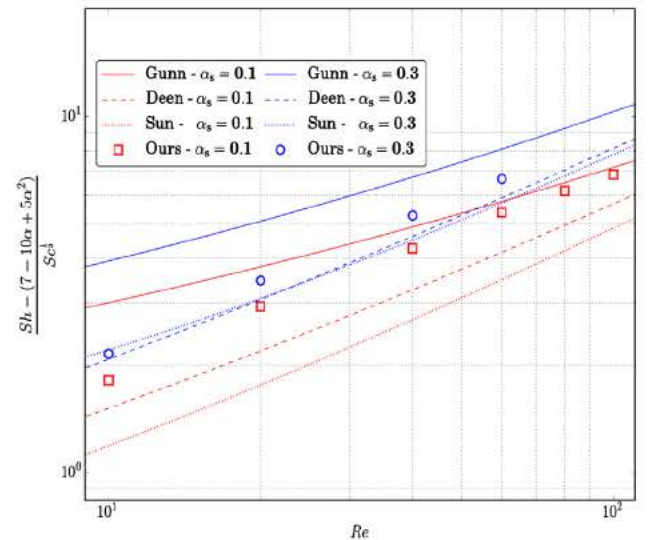


Fig. 3. Comparison of Sherwood number in a random array of particles for external mass transfer with correlations of Gunn (1978), Sun et al. (2016) and Deen et al. (2014).

$$Sh = \frac{(7 - 10\alpha_f + 5\alpha_f^2)(1 + 0.7Re^{0.2}Sc^{1/3})}{1 + (1.33 - 2.4\alpha_f + 1.2\alpha_f^2)Re^{0.7}Sc^{1/3}} \quad (18)$$

We can notice that the numerical simulation results get closer to those of (Gunn, 1978) for both  $\alpha_s$  when  $Re$  increases.

We show in Fig. A2 (g), (h) and (i) the concentration isosurfaces at infinite reaction rate corresponding to  $\alpha_s = 0.1$  and  $Re = 1, 10$  and 50, respectively.

### 3.2. Reactive mass transfer: single particle system

We consider a single catalyst particle placed in a convective diffusive fluid stream. The particle experiences internal diffusion coupled to a first order irreversible reaction. The interface conditions of the system are prescribed in (7) and (8). The rest of this section has been detailed in (Sulaiman et al., 2019a) and is summarized below for the sake of completeness. In (Sulaiman et al., 2019a), the mean particle surface concentration was established as follows:

$$\bar{C}_s = \frac{C_\infty}{1 + \frac{\gamma}{Sh} \left( \frac{\phi}{\tanh(\phi/2)} - 2 \right)} \delta C_\infty \quad (19)$$

Assuming constant  $C_s$ , the analytical concentration profile inside the particle is given by:

$$C(r^*) = C_s \frac{r_p^* \sinh(\phi r^*)}{r^* \sinh(\phi r_p^*)} \quad (20)$$

The mean volume concentration of the particle is obtained by integrating (20)

$$\bar{C}_v \simeq \frac{3}{4\pi r_p^{*3}} \int_0^{2\pi} \int_{\pi/2}^{+\pi/2} \int_0^{r_p^*} C_s(\phi, \theta) \times \frac{r_p^* \sinh(\phi r^*)}{r^* \sinh(\phi r_p^*)} \sin(\theta) r^{*2} d\phi d\theta dr^* \quad (21)$$

Assuming  $C_s$  uniform over the particle surface, we further approximate the integral as:

$$\bar{C}_v \simeq \frac{3\bar{C}_s}{4\pi r_p^{*3}} \int_0^{2\pi} \int_{\pi/2}^{+\pi/2} \int_0^{r_p^*} \frac{r_p^* \sinh(\phi r^*)}{r^* \sinh(\phi r_p^*)} \sin(\theta) r^{*2} d\phi d\theta dr^* \quad (22)$$

$$\frac{6\bar{C}_s}{\phi} \left( \frac{1}{\tanh(\phi/2)} - \frac{2}{\phi} \right) \beta \bar{C}_s$$

$\bar{C}_s$  is estimated by (19) and eventually the mean volume concentration  $\bar{C}_v$  reads as follows:

$$\bar{C}_v = \frac{6C_\infty}{1 + \frac{\gamma}{Sh} \left( \frac{\phi}{\tanh(\phi/2)} - 2 \right)} \left( \frac{1}{\phi \tanh(\phi/2)} - \frac{2}{\phi^2} \right) \delta \beta C_\infty \quad (23)$$

with  $Sh$  is the external Sherwood number. This assumption was validated in (Sulaiman et al., 2019a) for the single particle case, and in (Sulaiman et al., 2019b) for three interacting particles. In the previous cases, the particle  $Sh$  was evaluated through previously established correlations, such as (Feng and Michaelides, 2000).

### 3.3. Random assembly of reactive fixed particles

We now consider a system with many particles. All particles have the same physical properties and they are randomly distributed, forming a porous network through which the fluid flows. The individual rate of transfer is unknown in this case as the far field or bulk concentration is non uniform. The bulk concentration  $C(z)$  varies along the  $z$  direction for a network of particles due to the consumption of the chemical species as shown in Fig. 4.

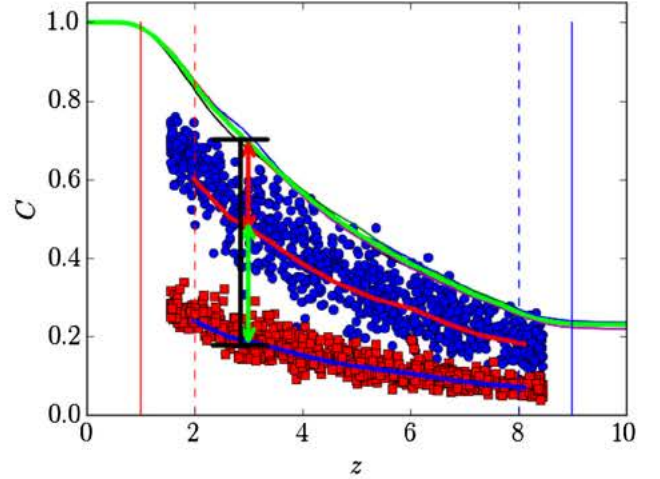


Fig. 4. Concentration profiles along the height of the domain. Green continuous line corresponds to cup-mixing concentration, red line corresponds to average of mean surface concentration and blue line to average of mean volume concentration. Disks correspond to mean surface concentration  $\bar{C}_s$  and squares correspond to mean volume concentration  $\bar{C}_v$ . Red vertical arrow shows  $\Delta \bar{C}_s(z) = \bar{C}(z) - \bar{C}_s(z)$ , black bar shows  $\Delta \bar{C}_v(z) = \bar{C}(z) - \bar{C}_v(z)$  and the green vertical arrow shows  $\bar{C}_s(z) - \bar{C}_v(z)$ . (For interpretation of the references to color in this figure legend, the reader is referred to the web version of this article.)

Thus, the cup mixing, the mean surface and the mean volume concentration profiles need to be predicted along  $z$  in order to be able to calculate the internal and external concentration difference. We propose a model using the analogy with the single particle system (19). The key point of the model is to predict the internal and external concentration differences. The external difference is  $\Delta \bar{C}_s(z) = \bar{C}(z) - \bar{C}_s(z)$ , between the average cup mixing and mean particle surface concentration. The internal difference between the cup mixing and mean volume concentration is  $\Delta \bar{C}_v(z) = \bar{C}(z) - \bar{C}_v(z)$ . We assume that the mean surface concentration of all the particles at a position  $z$  is approximated as:

$$\bar{C}_s(z) = \frac{\bar{C}(z)}{1 + \frac{\gamma}{Sh} \left( \frac{\phi}{\tanh(\phi/2)} - 2 \right)} \delta \bar{C}(z) \quad (24)$$

$Sh$  is the external Sherwood number that can be determined from mass transfer controlled system ( $Da \rightarrow \infty$ ) in a bed of particles. In a single particle system, it was evaluated through existing correlations such as (Feng and Michaelides, 2000) while for a multi particle system it can be estimated from correlations of (Gunn, 1978) or (Deen et al., 2014) as previously discussed.

Assuming negligible axial dispersion, the equation prescribing the cup mixing concentration profile along the  $z$  direction, taking into account the variation of the particle surface concentration along  $z$ , writes as follows:

$$\frac{d\bar{C}(z)}{dz} + \xi (\bar{C}(z) - \bar{C}_s(z)) = 0 \quad (25)$$

Taking into account the relation in (24), the equation can further be written as:

$$\frac{d\bar{C}(z)}{dz} + \xi(1 - \delta)\bar{C}(z) = 0 \quad (26)$$

The cup mixing concentration profile  $\bar{C}(z)$ , accounting for the evolution of the particle concentration as function of  $z$ , is simply the solution of (26) and reads as follows:

$$\bar{C}(z) = C_\infty \exp(-\xi(1 - \delta)z) \quad (27)$$

Note that we assumed  $\delta$  to be constant,  $0 < \delta < 1$ . For very slow reaction, i.e.  $Da \ll 1, \delta \rightarrow 1$ . For very fast reaction i.e.  $Da \rightarrow \infty, \delta \rightarrow 0$  and (27) is equivalent to (17) with  $C_s \rightarrow 0$ .  $\xi$  is the external mass transfer coefficient defined in (16) and is assumed to be independent of reaction rate. To verify the validity of the assumption that the external mass transfer coefficient is independent of  $Da$ , we recast (25) in the following form:

$$\xi = \frac{1}{(\bar{C}(z) - \bar{C}_s(z))} \frac{d\bar{C}(z)}{dz} \quad (28)$$

We compute  $\xi$  from numerical simulation results for three values of  $Da$  ( $Da = 40, Da = 200$ , and  $Da = \infty$ ) with  $\alpha_s = 0.5, Re = 10, Sc = 5$  and  $\gamma = 0.1$ . We compare in Table 2 the *min*, *max*, *mean* and the standard deviation  $\sigma$  of  $\xi$  along  $z$ . The average value of  $\xi$  is almost the same for  $Da = 40$  and  $Da = 200$ , with slight decrease for  $Da = \infty$ . The calculated results show fluctuations with a standard deviation below 20% or more precisely 12.7% for  $Da = 40$ , 12.6% for  $Da = 200$  and 16% for  $Da = \infty$ . This also validates that the assumption of negligible axial dispersion of concentration is valid for  $Re = 10$ . For higher Reynolds number flows, this assumption will become even more valid.

Now, the mean volume concentration profile along the height  $z$ , can be deduced from (22) and (24) as:

$$\bar{C}_v(z) = \bar{C}(z)\delta\beta \frac{\bar{C}(z)}{1 + \frac{\gamma}{Sh} \left( \frac{\phi}{\tanh(\phi/2)} - 2 \right)} \left( \frac{6}{\phi \tanh(\phi/2)} - \frac{12}{\phi^2} \right) \quad (29)$$

Thus, the cup mixing concentration profile, the mean surface concentration and the mean volume concentration are determined along the height  $z$  by (27), (24) and (29), respectively.

#### 4. Numerical simulation results

We perform SIM DLM/FD numerical simulations to validate the model. In this case, we set the simulation domain to:  $L_x = L_y = 6, L_z = 10$ , and  $\Delta l = 1$ . The spatial numerical resolution is increased to  $N_p = 40$  points per particle diameter to increase spatial resolution of boundary layers which are getting thinner with chemical reaction. According to our previous convergence study, performed in (Sulaiman et al., 2019b) for  $\gamma = 0.1$ , the numerical error on the surface concentration for the highest  $Da$  is less than 5%. All simulations are performed with  $CFL < 0.25$  to reach steady state. All numerical simulation results will be compared to the theoretical modeling in order to test its validity and dependence upon the five dimensionless parameters over the following ranges:

- $\alpha_s \in [0.1, 0.5]$
- $Re \in [1, 50]$
- $Sc \in [1, 10]$
- $Da \in [40, \infty]$
- $\gamma \in [10^{-2}, 10]$

**Table 2**

Statistics on the variation of  $\xi$  along  $z$  for three values of  $Da$ ,  $\alpha_s = 0.5, Re = 10, Sc = 5$  and  $\gamma = 0.1$ .

	$Da$		
$\xi$	40	200	$\infty$
<i>mean</i>	0.345	0.341	0.33
<i>min</i>	0.332	0.328	0.312
<i>max</i>	0.376	0.371	0.367
$\sigma$	0.013	0.013	0.016

The range of parameters corresponds to gas solid systems at low to moderate Reynolds number in order for the flow to remain steady. The ratio of diffusion coefficients models the effects of porosity and tortuosity of the particle micropores. The Schmidt number is limited to 10 because of numerical constraints (higher Schmidt number typical of liquid solid systems would lead to much thinner mass boundary layer). The range of Schmidt numbers  $[1, 10]$  considered corresponds, e.g., naphthalene air system ( $Sc = 2.5$ ). We compare the predictions of the model for the concentration profiles  $\bar{C}(z)$ ,  $\bar{C}_s(z)$ , and  $\bar{C}_v(z)$ , corresponding to (27), (24) and (29), respectively, with our numerical results.

We compute  $\bar{C}_s(z)$  numerically by sub dividing the bed along  $z$  into 10 slabs, indexed by  $i, i$  from 1 to 10. In slab  $i$ , we define  $n$  as the number of particles whose centers lie in the slab,  $\bar{C}_{spj}$  the mean surface concentration of a particle  $j$  ( $j$  from 1 to  $n$ ), and  $\bar{z}_{spj}$  the average particle position along  $z$ . We compute the average of mean surface concentration of all the particles in the slab  $i$  as follows:

$$\bar{C}_{si} = \frac{1}{n} \sum_{j=1}^n \bar{C}_{spj} \quad (30)$$

We compute the corresponding  $\bar{z}_{si}$  position for  $\bar{C}_{si}$  as follows:

$$\bar{z}_{si} = \frac{1}{n} \sum_{j=1}^n \bar{z}_{spj} \quad (31)$$

We follow the same procedure for the calculation of the average of mean volume concentration. For each case, we take the average of the five simulations corresponding to different random particle assemblies.

We consider three values for solid volume fraction;  $\alpha_s = 0.1$  (55 particles),  $\alpha_s = 0.3$  (165 particles) and  $\alpha_s = 0.5$  (275 particles), i.e., from a semi dilute regime to a rather dense regime.

##### 4.1. Dilute regime ( $\alpha_s = 0.1$ )

We present different cases with increasing effect of convection, the Reynolds number is varying from 1 to 10 while Schmidt number is either equal to 1 or 10. For each configuration, the effect of the kinetics of the chemical reaction is tested with two values of Damköhler number  $Da = 40$  and  $Da = 200$ . Finally, we investigate the modulation of mass transfer rate by the ratio of diffusion coefficients  $\gamma$ .

- Case A, we fix  $\gamma = 0.1, Re = 1, Sc = 1$  for two values of  $Da : Da = 40$  and  $Da = 200$ .
- Case B, we fix  $\gamma = 0.1, Re = 1, Sc = 10$  for two values of  $Da : Da = 40$  and  $Da = 200$ .

In case A, we compare the models at low  $Re$ , low  $\alpha_s$  and low  $Sc$ . We only vary  $Da$ . Then, in case B, the value of  $Sc$  is increased from 1 to 10, with respect to case A, which leads to higher Peclet number ( $Pe = Re.Sc$ ). We show the comparison between the predictions of our model and our numerical simulation results in Fig. 5 for the two cases. The predictions of our model compare well with our numerical results with a weaker agreement when  $Sc = 10$  and  $Da = 200$ , corresponding to thin external and internal boundary layers which scale with  $Sc^{-1/3}$  and  $Da^{-1/2}$ , respectively. It is clear that the observed discrepancy is stronger on profiles of  $\bar{C}_s(z)$  and more specifically when both  $Sc$  and  $Da$  are large (the largest discrepancy being below 20%).

- Case C, we fix  $\gamma = 0.1, Re = 10, Sc = 1$  for two values of  $Da : Da = 40$  and  $Da = 200$ .
- Case D, we fix  $\gamma = 0.1, Re = 10, Sc = 10$  for two values of  $Da : Da = 40$  and  $Da = 200$ .

In cases C and D, we only increase the value of  $Re$  from 1 to 10.

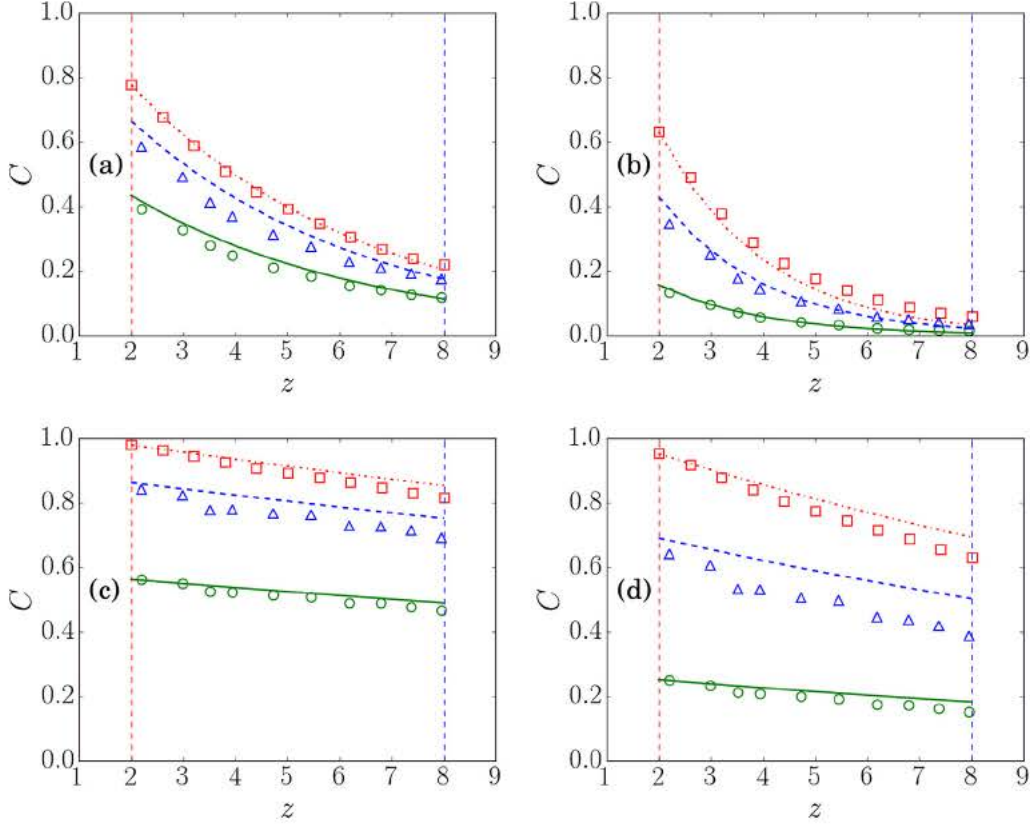


Fig. 5. Comparison of model prediction to numerical simulation results for  $\alpha_s = 0.1$ ,  $Re = 1$ , and  $\gamma = 0.1$ . Red color corresponds to  $\bar{C}(z)$ , blue color corresponds to  $\bar{C}_s(z)$  and green color corresponds to  $\bar{C}_v(z)$ . Lines stand for model and symbols for simulations. (a) and (b) correspond to  $Sc = 1$ , (c) and (d) correspond to  $Sc = 10$ , (a) and (c) correspond to  $Da = 40$  and (b) and (d) correspond to  $Da = 200$ . (For interpretation of the references to color in this figure legend, the reader is referred to the web version of this article.)

We show the comparison between the predictions of our model and our numerical simulation results in Fig. 6. The numerical results show a very good agreement between our model and the numerical results although the model overpredicts  $\bar{C}_s(z)$  in Fig. 6 a and b. Concentration profiles decrease with a lower slope along the height compared to cases A and B. This is due to the increase of convective effects induced by an increase of  $Re$  from 1 to 10. Mass transfer evolves with  $Re^{1/3}$  which enhances solute supply at particles interface and convective transport through the random assembly of particles. For case C, the concentration variation is very weak along the height. This is the result of great enhancement of the Peclet number ( $Pe = 500$ ) while reactive effect remains moderate.

- Case E, we fix  $\gamma = 0.1$ ,  $Re = 50$ ,  $Sc = 1$  for two values of  $Da$ :  $Da = 40$  and  $Da = 200$ .
- Case F, we fix  $\gamma = 0.1$ ,  $Re = 50$ ,  $Sc = 10$  for two values of  $Da$ :  $Da = 40$  and  $Da = 200$ .

In cases E and F, and with respect to cases C and D, we only increase the value of  $Re$  from 10 to 50. We show the comparison between the predictions of our model and our numerical simulation results in Fig. A1. The numerical results show a very good agreement between the predictions of our model and our numerical results. Concentration profiles decrease with a lower slope along the height than cases A, B, C and D which correspond to higher  $Pe$  number (e.g. 50 and 500). This is due to the increase of convective effects related to the increase of  $Re$  at constant reaction rate and constant solid volume fraction. At higher Peclet number,

the dimensionless transfer coefficient is expected to scale with  $Pe^{1/3}$ .

- Case G, we fix  $Re = 50$ ,  $Sc = 10$ , and  $Da = 40$  which corresponds to strong convection  $Pe = 500$  and moderate reaction kinetics. We vary  $\gamma$  such that  $\gamma \in [10^{-2}, 10^{-1}, 1, 10]$ .

Finally, in the dilute regime, we vary in case G the diffusion coefficient ratio  $\gamma$  ( $\gamma = 0.1$  was kept constant in all other simulations). For this case, we fix  $Re = 50$ ,  $Da = 40$ ,  $Sc = 10$ , and  $\alpha_s = 0.1$ . We compare the predictions of our model and our numerical results for four values of  $\gamma$ :  $10^{-2}$ ,  $10^{-1}$ , 1, and 10. We compare results in Fig. 7. For  $\gamma = 10^{-2}$  and  $\gamma = 10^{-1}$ , the predictions of our model show a very good agreement with our numerical simulation results. For  $\gamma = 1$ , numerical results show a systematic deviation from the predictions of the model. The difference between the predictions of the model and the numerical simulation results increases for  $\gamma = 10$ . It is markedly large for  $\bar{C}_s(z)$  which is under predicted by a factor almost 2. Increasing the diffusion coefficient ratio  $\gamma$  at a constant  $Da$  decreases the surface and mean volume concentration of the particles (see Fig. 8). However, this configuration of higher diffusion in particles is not likely to occur in practical applications.

In fact, decreasing the bulk diffusion coefficient decreases the supply of chemical species to particles, at a constant consumption rate of reaction. This is in line with what takes place when  $Re$  or  $Sc$  is decreased. Mathematically,  $\gamma$  tending to  $\infty$  in (24) or  $\phi = Da^{1/2}$  tending to  $\infty$  in (24) has the same effect. In both cases the particle surface concentration tends to zero and thus the internal boundary layer gets thinner.

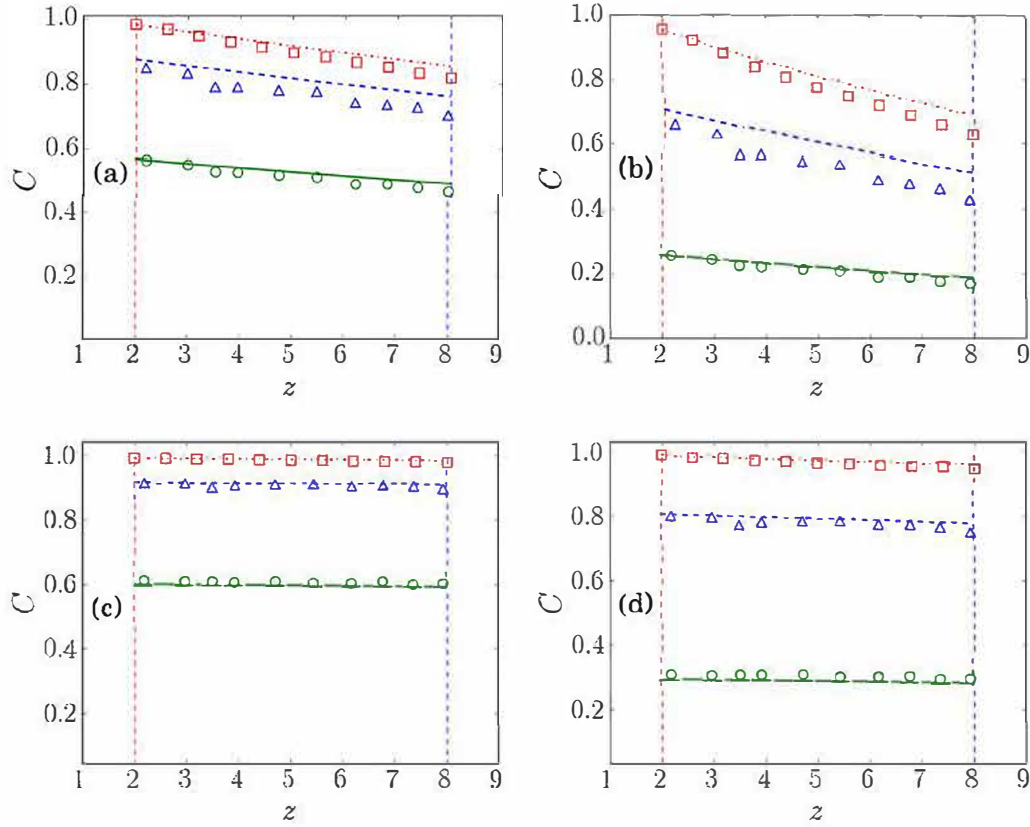


Fig. 6. Comparison of model prediction to numerical simulation results for  $\alpha_s = 0.1, Re = 10$ , and  $\gamma = 0.1$ . Red color corresponds to  $\bar{C}(z)$ , blue color corresponds to  $\bar{C}_s(z)$  and green color corresponds to  $\bar{C}_p(z)$ . Lines stand for model and symbols for simulations. (a) and (b) correspond to  $Sc = 1$ , (c) and (d) correspond to  $Sc = 10$ , (a) and (c) correspond to  $Da = 40$  and (b) and (d) correspond to  $Da = 200$ . (For interpretation of the references to color in this figure legend, the reader is referred to the web version of this article.)

In order to illustrate this observation, we arbitrarily select five particles in the assembly and we plot their internal concentration profiles for  $\gamma = 10^{-2}, \gamma = 1$  and  $\gamma = 10$  in Fig. 9. When the diffusion ratio is lower than one, it models the reduction of the diffusion coefficient due to confinement in the micropores of the porous catalyst particle. Increasing the diffusion ratio above one shifts progressively the main resistance to transfer from the internal to external boundary layer. We give information on the positions of the selected particles in Table 3.

Particles show approximately a similar concentration profile for the same  $\gamma$  for all positions. However, when  $\gamma$  increases, the surface concentration significantly decreases with an increase of the gradient between the surface and bulk concentrations. This explains the increase of the numerical error and thus the model cannot be tested in this case as the simulations are not well spatially resolved. The concentration iso contours of this case are shown in Fig. 8. They clearly show the decrease of the particle concentration with an increase of  $\gamma$ . This observation is similar to what we can see in Fig. 11, where we compare the concentration iso contours for another case at  $Re = 25, \gamma = 0.1, Sc = 10, \alpha_s = 0.3$  and many  $Da$ . We show in Fig. A2 the concentration iso surfaces for  $\alpha_s = 0.1, \gamma = 0.1$  and  $Sc = 1$ . In (a), (b) and (c), we increase  $Re$  from 1, to 10 and 50 respectively, at a constant  $Da$ . The concentration increases with the increase of  $Re$ . As previously pointed out, the increase of  $Re$  increases the convective effects and solute supply at constant consumption rate. In Fig. A2 (c), (f), and (i),  $Re$  is fixed to 50 and the reaction rate increases such that  $Da = 40, 200$  and  $\infty$ . The mean solute concentration in particles as well as the mean concentration in the fluid decrease with an increase of  $Da$ . At a constant supply rate through convection and mass diffusion, the consumption of the chemical species due to

reaction has been increased. The increase of  $Da$  increases significantly the slope of concentration gradients near particle surfaces. This is the reason why we selected  $N_p = 40$  grid points per particle diameter in order to accurately capture the correct boundary layers (while for external mass transfer only  $N_p = 24$  was sufficient for a similar level of accuracy). Thus, we infer that the discrepancy between the model and simulations when we increase  $\gamma$  is due to the numerical spatial resolution.

#### 4.2. Moderately concentrated regime ( $\alpha_s = 0.3$ )

- Case H, we fix  $\gamma = 0.1, Re = 10, Sc = 1$  for two values of  $Da$ :  $Da = 40$  and  $Da = 200$ .
- Case I, we fix  $\gamma = 0.1, Re = 10, Sc = 10$  for two values of  $Da$ :  $Da = 40$  and  $Da = 200$ .

In cases H and I, we only increase the solid volume fraction  $\alpha_s$  from 0.1 to 0.3 with respect to cases C and D. Increasing the solid fraction in the bed yields reduction of the mean interparticle distance which scales with  $\alpha_s^{-1/3}$ . We show the comparison between the predictions of our model and our numerical results in Fig. 10. The numerical simulation results show a good agreement between the predictions of our model and our numerical results for  $Sc = 1$  although it is clear that the discrepancy is stronger on profiles of  $\bar{C}_s(z)$ . The agreement gets better for  $Sc = 10$ . The physical explanation of this observation is that when the convective effects increase, the particle surface concentration gets more uniform, and so, the assumptions made to obtain (24) are more valid. Indeed, for a given particle in the bed, neighboring particles induce heterogeneity to its surrounding concentration field. The increase of  $Re$  or  $Sc$ , consequently  $Pe = Re \cdot Sc$ , enhances the uniformity of

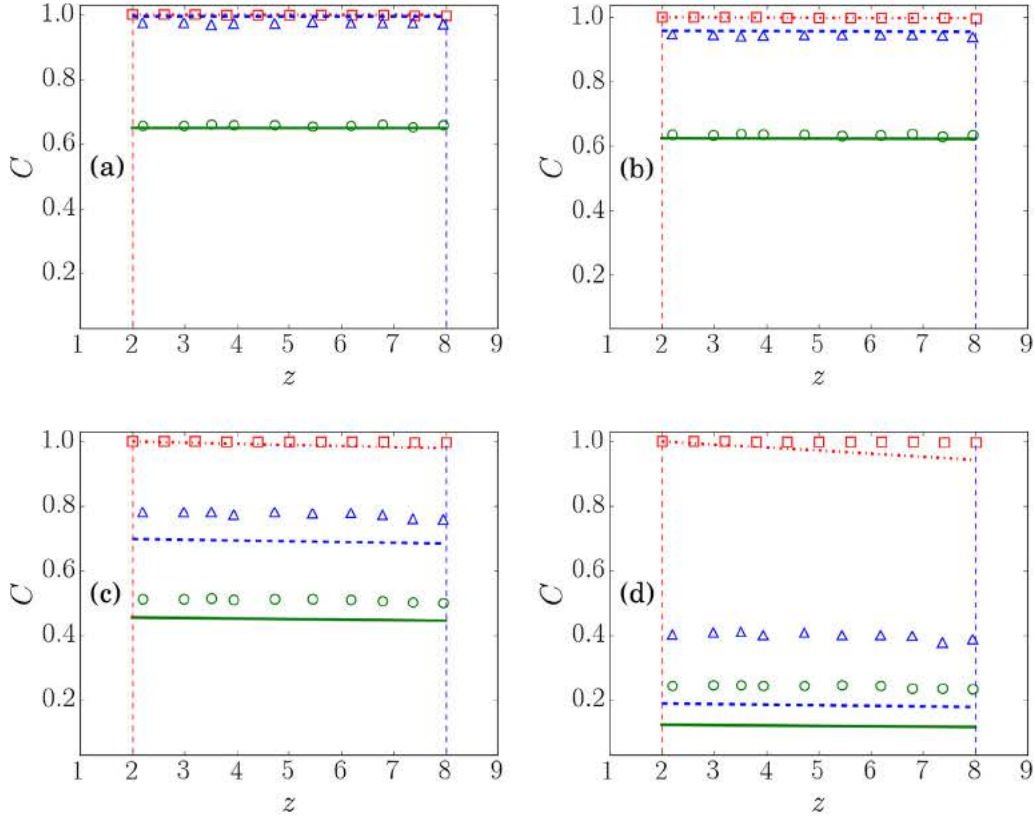


Fig. 7. Comparison of model prediction to numerical simulation results for  $\alpha_s = 0.1, Re = 50$ , and  $Da = 40$ . Red color corresponds to  $\bar{C}(z)$ , blue color corresponds to  $\tilde{C}_s(z)$  and green color corresponds to  $\tilde{C}_p(z)$ . Lines stand for model and symbols for simulations. (a) corresponds to  $\gamma = 0.01$ , (b) corresponds to  $\gamma = 0.1$ , (c) corresponds to  $\gamma = 1$  and (d) corresponds to  $\gamma = 10$ . (For interpretation of the references to color in this figure legend, the reader is referred to the web version of this article.)

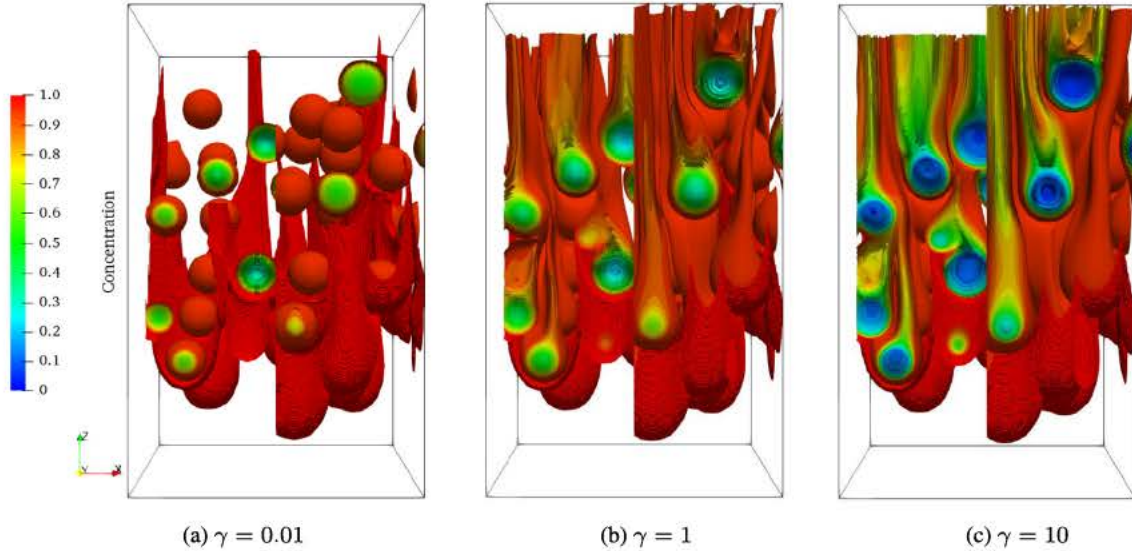


Fig. 8. Concentration contours at  $Re = 50, Sc = 10, Da = 40, \alpha_s = 0.1, \gamma = 10^{-2}, 1$  and  $10$ .

the concentration field. Assuming  $Pe \rightarrow \infty$ , the concentration field around the particle will be uniform and equal to the inlet concentration  $C_\infty$ .

Concentration profiles decrease with a lower slope along the height than in cases C and D. This is due to the increase of the number of particles per volume of reactor and consequently an increase of the specific surface available for chemical reaction which induces stronger consumption of the solute concentration. An

increase of the reaction kinetics yield significant local inhomogeneities of concentration distribution across the bed (see Fig. 11).

#### 4.3. Dense regime ( $\alpha_s = 0.5$ )

- Case J, we fix  $\gamma = 0.1, Re = 1, Sc = 1$  for two values of  $Da$ :  $Da = 40$  and  $Da = 200$ .

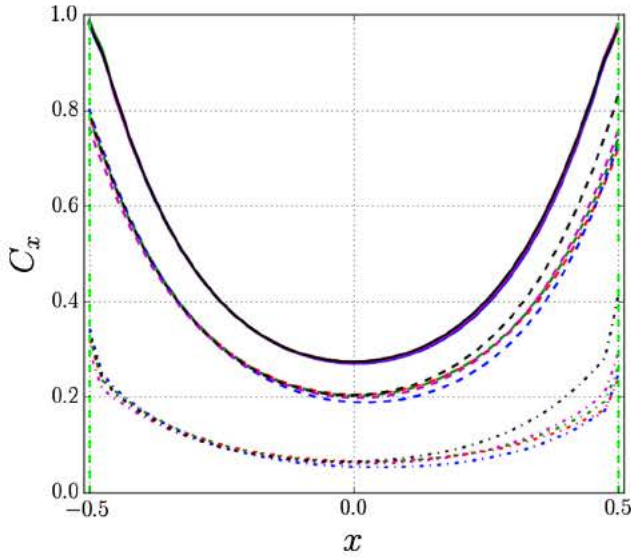


Fig. 9. Concentration profiles across the diameter of selected particles in Table 3. Continuous lines correspond to  $\gamma = 10^{-2}$ , dashed lines correspond to  $\gamma = 10^{-1}$  and dotted lines correspond to  $\gamma = 10^{-3}$ . Colors: magenta, blue, green, black, and red correspond to particles (a), (b), (c), (d), and (e), respectively. (For interpretation of the references to color in this figure legend, the reader is referred to the web version of this article.)

Table 3  
Positions of selected particles in the bed for concentration profiles comparison shown in Fig. 9.

Particle	Position		
	$x/d$	$y/d$	$z/d$
a	4.872	2.499	1.701
b	5.706	4.04	3.309
c	5.948	5.500	5.946
d	5.933	3.611	7.057
e	2.411	2.334	7.447

- Case K, we fix  $\gamma = 0.1, Re = 1, Sc = 10$  for two values of  $Da : Da = 40$  and  $Da = 200$ .

Cases J and K are similar to cases A and B, but with an increase of the solid volume fraction  $\alpha_s$  from 0.1 to 0.5. We show the comparison between the predictions of our model and our numerical simulation results in Fig. 12. The results show a good agreement between the predictions of our model and our simulation numerical results for both  $Sc = 1$  and  $Sc = 10$  (the discrepancy is stronger on profiles of  $\bar{C}_s(z)$  when the  $Sc$  number is large). However, model predictions are better for cases A and B (where  $\alpha_s = 0.1$ ). When solid volume fraction increases, the surface concentration of a given particle experiences non uniform spatial distribution of the surrounding concentration field. The presence of many neighboring particles strongly disturbs the concentration field and so the assumption made in (24) is less valid. This is especially significant when convective effects are weak corresponding to thick boundary layers. Concentration profiles in these cases show a steeper slope along the height than in cases A and B. This is due to an increase of number of particles and consequently an increase of the mean consumption rate of the chemical species over a certain height.

- Case L, we fix  $\gamma = 0.1, Re = 10, Sc = 1$  for two values of  $Da : Da = 40$  and  $Da = 200$ .
- Case M, we fix  $\gamma = 0.1, Re = 10, Sc = 5$  for two values of  $Da : Da = 40$  and  $Da = 200$ .

Cases L and M are similar to cases J and K, with an increase of  $Re$  from 1 to 10. (Note that  $Sc = 5$  in case M whereas  $Sc = 10$  in case K.) We show the comparison between the predictions of our model and our numerical results in Fig. 13.

The numerical simulation results show an overall good agreement between the predictions of our model and our numerical results for both  $Sc = 1$  and  $Sc = 5$  while the discrepancy is stronger on profiles of  $\bar{C}_s(z)$ . However, the predictions of the model are better in cases L and M than in cases J and K. For a given solid volume fraction, the particle surface concentration becomes more uniform when the convective effects increase. The increase of the convective effects enhances the spatial homogeneity of the concentration field and reduces the disturbances induced by neighboring particles. Hence, the assumption made in (24) is more valid. Concentration profiles have a lower slope along the bed height than in cases J and K. This is due to the increase of convective supply of chemical species to the particles surface at a constant consumption rate.

- Case N, we fix  $\gamma = 0.1, Re = 25, Sc = 1$  for two values of  $Da : Da = 40$  and  $Da = 200$ .
- Case O, we fix  $\gamma = 0.1, Re = 25, Sc = 10$  for two values of  $Da : Da = 40$  and  $Da = 200$ .

Cases N and O are similar to cases L and M, with only an increase of  $Re$  from 10 to 25. (Note that  $Sc = 10$  in case O whereas  $Sc = 5$  in case M.) We show the comparison in Fig. A3. We observe a good agreement between the predictions of our model and our numerical simulation results for both  $Sc = 1$  and  $Sc = 5$  although the prediction of profiles of  $\bar{C}_s(z)$  is less accurate. However, the predictions of the model are almost similar to those in cases L and M although a systematic overestimate of  $\bar{C}_s(z)$  is observed. Increasing convective effects does not change the level of agreement between the predictions of the model and the numerical simulation results. In all cases where  $\alpha_s = 0.5$ , the agreement between the predictions of the model and the numerical results is weaker. The assumptions are less valid at high solid volume fraction. Particles may experience, in this case, strong spatial concentration variations over their surfaces due the disturbance induced by neighboring particles. Serious limitations of the model were expected in this case due to strong inhomogeneities of the concentration field across the assembly of particles.

## 5. Dimensionless mass transfer coefficient

### 5.1. Reactive Sherwood number

For a single particle, the mass transfer coefficient that accounts for all the effects in the system can be obtained through the additivity rule. The rule states that the total resistance to mass transfer in the system can be considered as a sum of two resistances in series. The first resistance is the inverse of the internal mass transfer coefficient  $k_{in}^*$  in the solid phase, and the second resistance is the inverse of the external transfer coefficient  $k_f^*$  in the fluid phase. The total mass transfer coefficient  $k^*$ , via the additivity rule, writes as:

$$\frac{1}{k^*} = \frac{1}{k_{in}^*} + \frac{1}{k_f^*} \quad (32)$$

We consequently introduce two Sherwood numbers as:

- internal Sherwood number  $Sh_{in}$

$$Sh_{in} = \frac{N_{s, \partial P}^* d_p^*}{D_s^* \left( \bar{C}_s - \bar{C}_v \right)} = \frac{k_{in}^* d_p^*}{D_s^*} \quad (33)$$

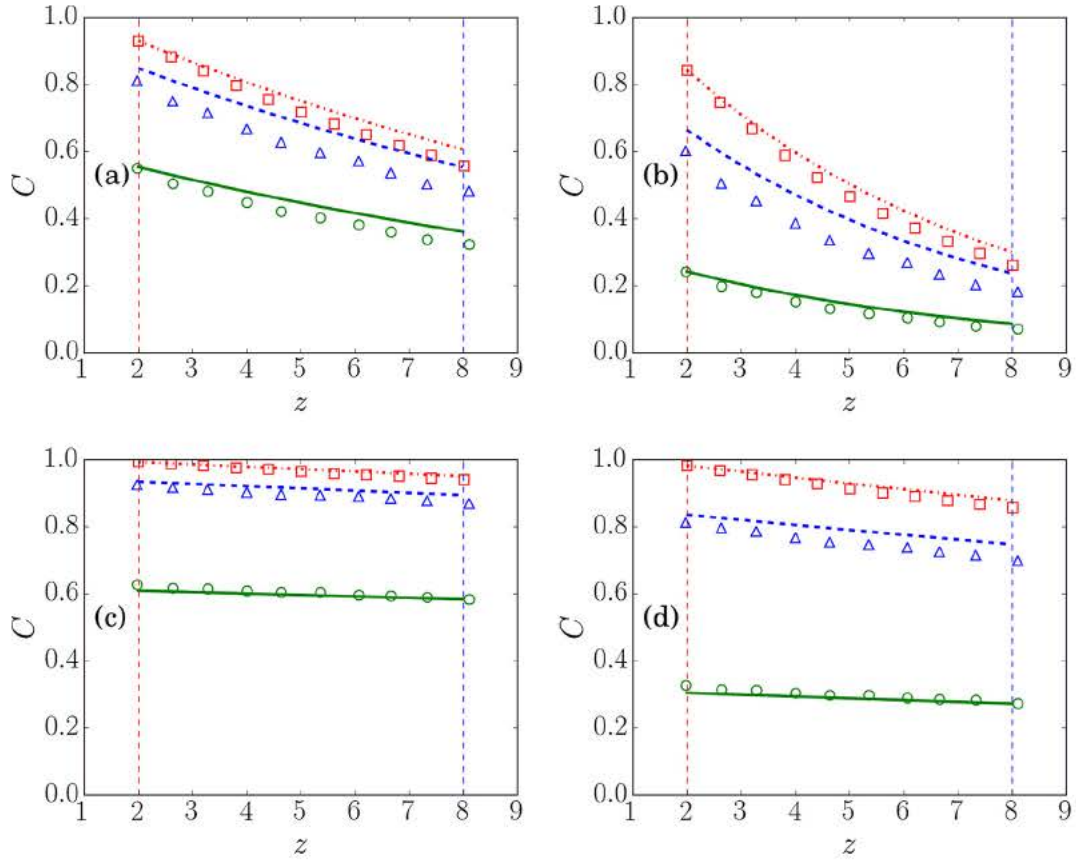


Fig. 10. Comparison of model prediction to numerical simulation results for  $\alpha_s = 0.3, Re = 10$ , and  $\gamma = 0.1$ . Red color corresponds to  $\bar{C}(z)$ , blue color corresponds to  $\tilde{C}_s(z)$  and green color corresponds to  $\tilde{C}_p(z)$ . Lines stand for model and symbols for simulations. (a) and (b) correspond to  $Sc = 1$ , (c) and (d) correspond to  $Sc = 10$ , (a) and (c) correspond to  $Da = 40$  and (b) and (d) correspond to  $Da = 200$ . (For interpretation of the references to color in this figure legend, the reader is referred to the web version of this article.)

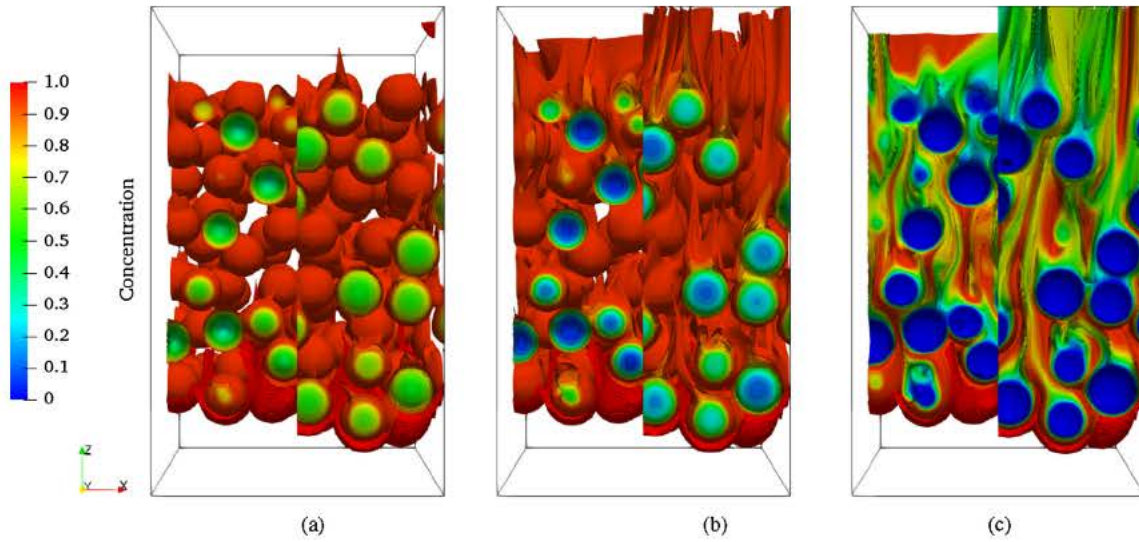


Fig. 11. Concentration contours at  $Re = 25, \gamma = 0.1, \alpha_s = 0.3$  with (a)  $Da = 40$ , (b)  $Da = 200$  and (c)  $Da = \infty$ .

- external Sherwood number  $Sh$

$$Sh = \frac{N_{f,op}^* d_p^*}{D_f^* (C_\infty - C_s)} = \frac{k_f^* d_p^*}{D_f^*} \quad (34)$$

We reformulate (32) in terms of Sherwood numbers. The global Sherwood number for an isolated particle  $\widetilde{Sh}_0 = \frac{k_f^* d_p^*}{D_f^*}$ , is obtained from:

$$\frac{1}{\widetilde{Sh}_0} = \frac{1}{\gamma Sh_{in}} + \frac{1}{Sh} \quad (35)$$

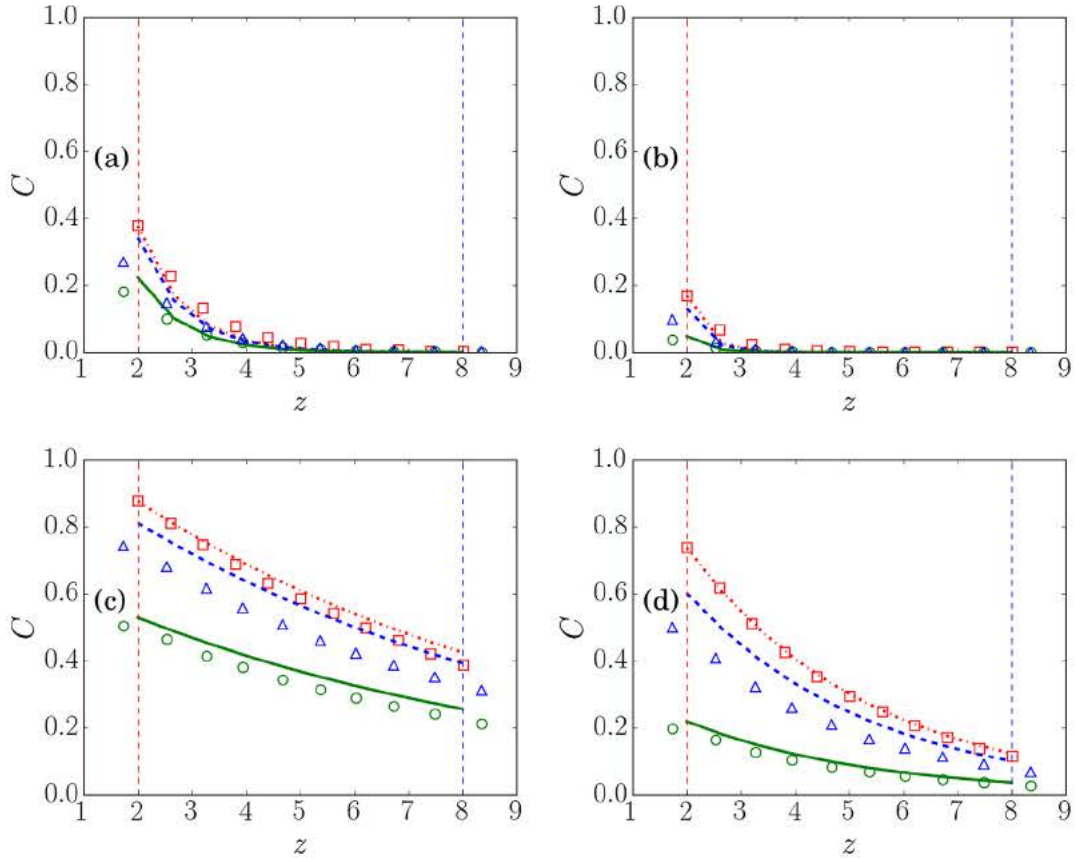


Fig. 12. Comparison of model prediction to numerical simulation results for  $\alpha_s = 0.5, Re = 1$ , and  $\gamma = 0.1$ . Red color corresponds to  $\bar{C}(z)$ , blue color corresponds to  $\bar{C}_s(z)$  and green color corresponds to  $\bar{C}_v(z)$ . Lines stand for model and symbols for simulations. (a) and (b) correspond to  $Sc = 1$ , (c) and (d) correspond to  $Sc = 10$ , (a) and (c) correspond to  $Da = 40$  and (b) and (d) correspond to  $Da = 200$ . (For interpretation of the references to color in this figure legend, the reader is referred to the web version of this article.)

$Sh$  was evaluated through previously established correlations, such as (Feng and Michaelides, 2000) for an isolated particle. The expression of  $\widetilde{Sh}_0$  can be written as function of  $Sh, \Delta \bar{C}_s, C_\infty, \bar{C}_s$  and  $\Delta \bar{C}_v, C_\infty, \bar{C}_v$ , using the continuity of the flux density at  $\partial P$ , it reads as follows:

$$\widetilde{Sh}_0 = Sh \frac{C_\infty}{C_\infty} \frac{\bar{C}_s}{\bar{C}_v} = Sh \frac{\Delta \bar{C}_s}{\Delta \bar{C}_v} \quad (36)$$

Using (19) and (22), the reactive Sherwood number  $\widetilde{Sh}_0$  of the single sphere system can be written as:

$$\widetilde{Sh}_0(Re, Sc, \phi, \gamma) = \frac{Sh(Re, Sc)}{\frac{Sh(Re, Sc)}{2\gamma} \left[ \frac{\tanh(\phi/2)}{\phi/2} \frac{12}{\phi^2} \right] + 1} \quad (37)$$

In the case of a bed of particles with solid concentration  $\alpha_s$ , the global mass transfer coefficient is obtained with

$$\widetilde{Sh}(Re, Sc, \phi, \gamma, \alpha_s) = Sh \frac{\Delta \bar{C}_s(z)}{\Delta \bar{C}_v(z)} = Sh \frac{\bar{C}(z)}{\bar{C}(z)} \frac{\bar{C}_s(z)}{\bar{C}_v(z)} = Sh \frac{\bar{C}(z)}{\bar{C}(z)} \frac{\delta \bar{C}(z)}{\delta \beta \bar{C}(z)} = Sh \frac{1}{1} \frac{\delta}{\delta \beta} \quad (38)$$

In the case of a bed of particles,  $Sh$  was obtained by our simulations with infinite  $Da$  (see for example Fig. 3) or can be approximated by correlation (18) of (Gunn, 1978). This expression accounts for the overall solid fraction  $\alpha_s$  in the bed but neglects direct particle interactions mediated by the fluid (all particles at a given height are assumed to have similar concentration).

This dimensionless coefficient includes the coupled effects of external diffusion convection and internal diffusion reaction on the overall mass transfer from the particles to the fluid. This can be used, for instance, as a closure law for reactive mass transfer simulations in DEM CFD (DEM stands for Discrete Element Methods) approaches for which mass balance equations are resolved at a much larger scale than the particle size. Our micro to meso scale modelling is tested under different configurations from the dilute to the dense regime. The expression of  $\widetilde{Sh}$  which formally does not depend on  $z$  is based on the assumption that all particles at the same height in the bed must behave uniformly (same surface concentration which is an assumption to be tested similarly to Table 2). We compare the reactive Sherwood number  $\widetilde{Sh}$  (38) with numerical simulations for four different cases with  $\gamma = 0.1$ :

- I:  $\alpha_s = 0.1$ , and  $Sc = 1$ .
- II:  $\alpha_s = 0.1$ , and  $Sc = 5$ .
- III:  $\alpha_s = 0.1$ , and  $Sc = 10$ .
- IV:  $\alpha_s = 0.5$ , and  $Sc = 10$ .

In the first three cases, I, II and III, we fixed  $\alpha_s = 0.1$  and  $Sc$  varies from 1 to 10. For each case we consider three values of  $Da$  (40, 200,  $\infty$ ) and two values of  $Re$  (10, 50). For the fourth case, IV, we consider  $\alpha_s = 0.5$  and  $Sc = 10$ , three values of  $Da$  (40, 200,  $\infty$ ) and two values of  $Re$  (10, 25). We show the results in Fig. 14. For the first three cases, I, II and III, the predictions of the model compare well with the numerical simulation results. However the predictions of the model are better in case II than in case I, and better in case III than in case II. In case IV, the predictions of the model

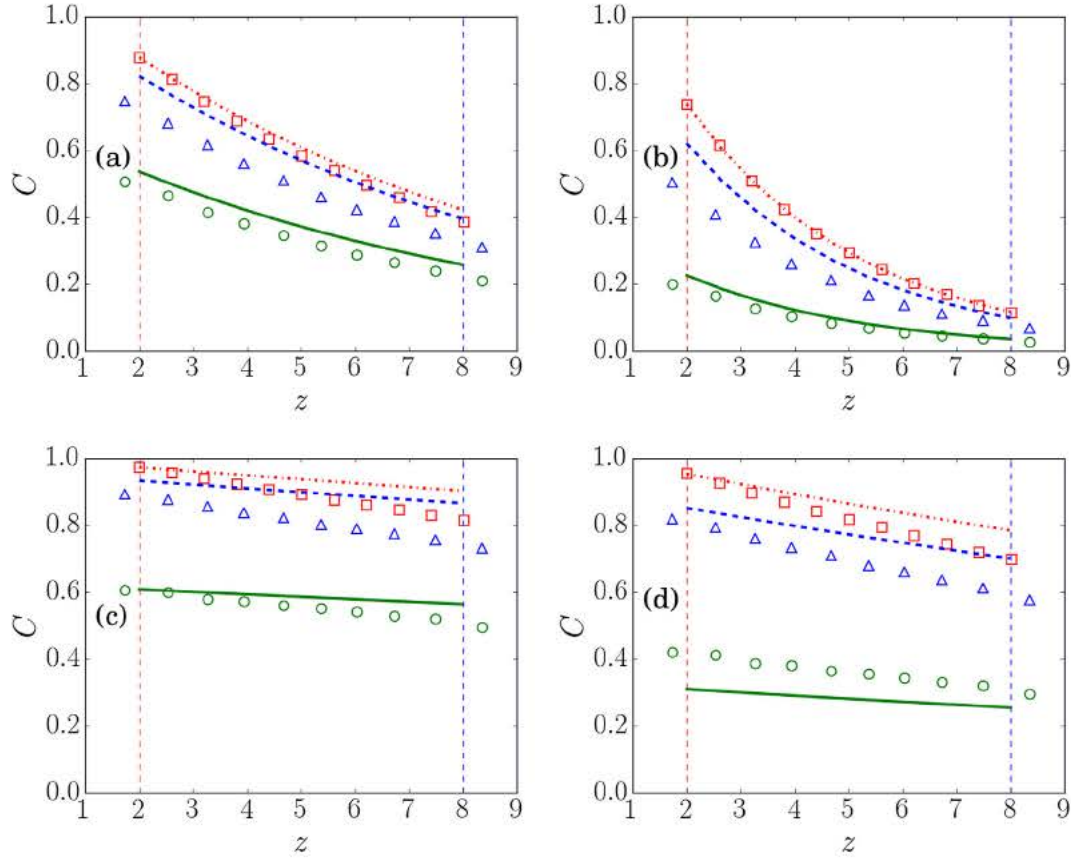


Fig. 13. Comparison of model prediction to numerical simulation results for  $\alpha_s = 0.5$ ,  $Re = 10$ , and  $\gamma = 0.1$ . Red color corresponds to  $\bar{C}(z)$ , blue color corresponds to  $\bar{C}_s(z)$  and green color corresponds to  $\bar{C}_v(z)$ . Lines stand for model and symbols for simulations. (a) and (b) correspond to  $Sc = 1$ , (c) and (d) correspond to  $Sc = 5$ , (a) and (c) correspond to  $Da = 40$  and (b) and (d) correspond to  $Da = 200$ . (For interpretation of the references to color in this figure legend, the reader is referred to the web version of this article.)

show a weaker agreement with the numerical results. Note that the only difference between case III and case IV is the solid volume fraction, i.e., otherwise all other dimensionless parameters are the same in both cases.

## 5.2. Discussion

The reactive Sherwood number is a dimensionless quantity characterizing the rate of mass transfer while a chemical reaction takes place within catalyst particles.

At high  $\alpha_s$  and low  $Pe$ , we observe that the semi-analytical predictive model shows limitations. The assumption for the prediction of the mean surface concentration of the particles is that the local particle surface concentration does not experience important variations due to hydrodynamic perturbations of surrounding particles (this is expected to be true for a dilute system). Consequently, the model is expected to show limitations when the local surface concentration of each particle is non-uniform due to local heterogeneity of the concentration spatial distribution generated by mass boundary layers and wakes. When the solid volume fraction increases, more particles are interacting with each other throughout the assembly. However, the homogeneity of the concentration spatial distribution is enhanced when  $Pe$  increases. Indeed, increasing  $Pe$  strengthens convective effects and consequently enhances supply of chemical species to the bed which is consumed by particles. Assuming an infinite flow rate (for any given  $\alpha_s$ ), the concentration field surrounding each particle will tend to uniform concentration  $C_f = C_\infty$ .

In order to elaborate on model limitations, we compute the standard deviation  $\sigma$  of the normalized cup mixing concentration

distribution (Eq. (39)) over the bed for two sets of simulation: varying  $Pe$  through different Reynolds number at  $Sc = 10$  and varying the solid volume fraction while other parameters are kept constant.

$$\kappa = \frac{C_f(x, y, z) - \bar{C}(z)}{\bar{C}(z)} \quad (39)$$

The mean of the standard deviation is formed over the five random seeding of particles and characterizes the homogeneity of the spatial distribution of solute concentration.

First, when the solid volume fraction is fixed,  $\alpha_s = 0.1$ , we investigate the effect of convection (see Table 4). For  $Re = 50$ , the standard deviation  $\sigma$  is very low corresponding to rather uniform distribution of the concentration. Reducing  $Re$  to 10 and 1,  $\sigma$  increases drastically. This emphasizes that the concentration field is getting more and more heterogeneous when  $Re$  decreases, as expected. The case  $Re = 10$  is illustrated on the left column of Fig. 15.

In the second set of simulations (see Table 5), we fix  $Re = 10$  and  $Sc = 10$  while the solid volume fraction is varied from dilute to dense regime. For  $\alpha_s = 0.1$ ,  $\sigma$  is small while it increases for  $\alpha_s = 0.3$ , and even more for  $\alpha_s = 0.5$ . This shows that the concentration field is getting more heterogeneous when the number of particles in the assembly increases and that inter-particle distance reduces. This results from direct pairwise or multi-body particle interactions mediated by the fluid flow. The concentration and velocity magnitude spatial distributions in a horizontal slice are shown at mid height,  $z = 5d$ , in Fig. 15, for  $Re = 10$ ,  $Sc = 10$ ,  $Da = 200$ ,  $\gamma = 0.1$  and two values of solid fraction

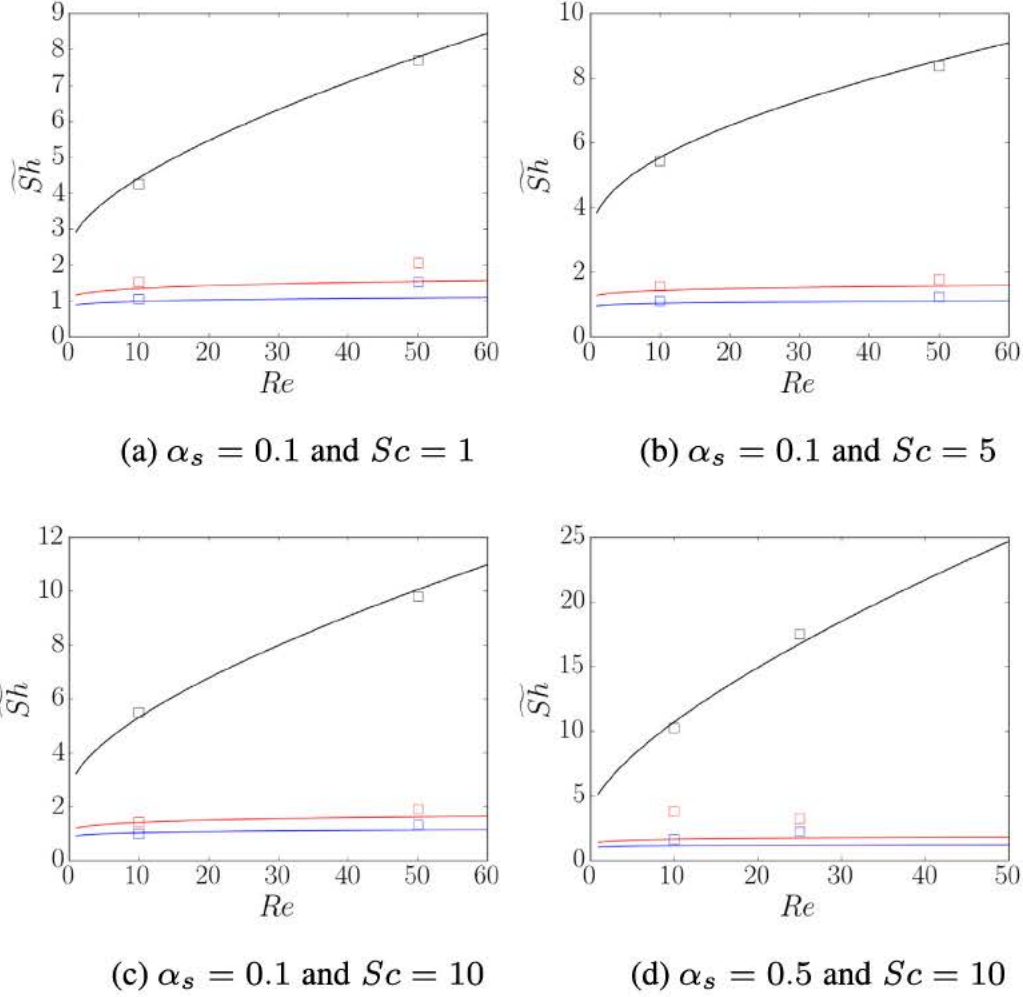


**Fig. 14.** Comparison of model prediction to numerical simulation results. (a), (b), (c), and (d) correspond to cases I, II, III, and IV, respectively. Colors blue, red and black correspond to  $Da = 40$ ,  $Da = 200$  and  $Da = \infty$ , respectively. Continuous lines represent model and symbols represent simulations. (For interpretation of the references to color in this figure legend, the reader is referred to the web version of this article.)

**Table 4**  
The standard deviation  $\sigma$  of (39) for  $\gamma = 0.1$ ,  $Da = 200$ ,  $\alpha_s = 0.1$ ,  $Sc = 10$  and different  $Re$  corresponding to  $Pe$  equal to 10, 100 and 500.

Configurations	$\sigma_{Re=1}$	$\sigma_{Re=10}$	$\sigma_{Re=50}$
Mean value	0.2474	0.1628	0.0936

$\alpha_s$  (0.1 and 0.3). We can clearly observe that the concentration field heterogeneity is increased when  $\alpha_s$  increases due to the presence of neighboring particles. The spatial distribution of the concentration for both  $\alpha_s$  is strongly correlated to the velocity magnitude which is enforced by the presence of no slip boundary condition on particle surfaces. In fact, this is a direct effect of the local microstructure of the assembly due to the relative position of particles. In the model, these direct hydrodynamic interactions are neglected and only the solid volume fraction is accounted for in the correlation.

## 6. Conclusion

We studied the effect of a first order irreversible chemical reaction on mass transfer through random assemblies of reactive spherical catalyst particles. We derived a theoretical model for the prediction of the cup mixing concentration profile of the fluid, the average of mean surface and the average of mean volume con-

centration profiles of the catalyst particles assuming axial dispersion is negligible. The model we proposed accounts for the effects of convection and diffusion in the fluid phase along with diffusion and chemical reaction in the solid phase. Under steady state, the model assumes that internal and external mass transfers can be coupled through continuity of concentration and flux density at the particle surface. Assuming constant and uniform concentration distribution along the surface of each particle, internal transfer coefficient is calculated through an analytic solution of diffusion reaction mass balance equation inside particles.

We performed particle resolved numerical simulations over a wide range of the five dimensionless parameters controlling the system ( $Re$ ,  $Sc$ ,  $\alpha_s$ ,  $\gamma$ ,  $Da$ ) and we compared the predictions of our model to our numerical simulation results. The model showed a very good ability to predict the correct concentration profiles resulting from numerical results. Also, the dimensionless mass transfer coefficient is well predicted by our model of 'reactive' Sherwood number. At a constant  $Pe$ , the model has proven to better predict the profiles when the solid volume fraction  $\alpha_s$  decreases. Conversely, at a constant  $\alpha_s$ , the predictions of the model improved when  $Pe$  increases.

The limitations of the model at high solid volume fraction and low convective effect arise from the fact that the model for the mean surface concentration of the particle was derived assuming that the particle surface concentration does not experience any sig-

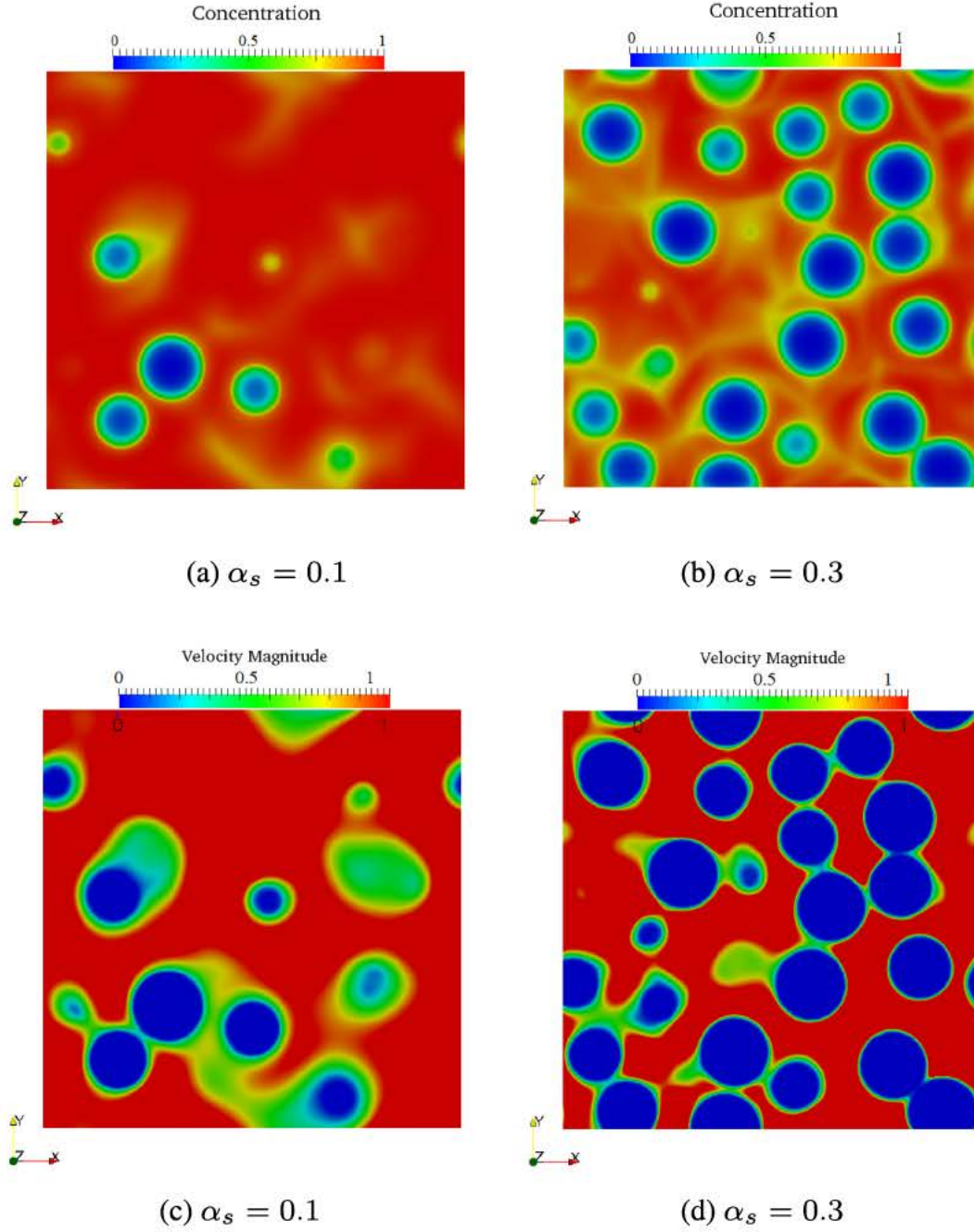


Fig. 15. Concentration spatial distribution (a and b) and their corresponding velocity magnitude (c and d) in the mid-plane  $z = 0.5$ , for  $\gamma = 0.1, Da = 200, Re = 10$  and  $Sc = 10$ .

**Table 5**  
The standard deviation  $\sigma$  of (39) for  $\gamma = 0.1, Re = 10, Da = 200, Sc = 10$  and different volume fractions  $\alpha_s$ .

Configuration	$\sigma_{\alpha_s=0.1}$	$\sigma_{\alpha_s=0.3}$	$\sigma_{\alpha_s=0.5}$
Mean value	0.072	0.259	0.7508

nificant spatial variation. This assumption has been shown to be valid for a system comprising a single particle or three interacting aligned particles, since the concentration field around each particle is quasi uniform in these cases. Moreover, it is assumed in the model that all particles at a certain height in the bed have the same concentration. Chemical species are consumed by the particles and in each wake there is a local reduction of solute concentration

which is transported by the fluid. When the solid volume fraction increases, more particles are present in the system, inducing heterogeneities to the concentration field due to their consumption of the chemical species transported by the fluid, that in turn affects negatively the surface concentration uniformity of particles. Indeed, at high concentration of particles local hydrodynamic interactions yield strong inhomogeneities of the solute concentration spatial distribution. The surface concentration on neighboring particles is strongly influenced by the local concentration variations in the bulk of the fluid. This is particularly true at low  $Pe$  number. This makes the assumption of uniform solute surface distribution far from being valid and flaws the prediction of the model. The local particle interactions mediated by the fluid makes the concentration of particles to be non uniform at a given height

while the model only accounts for the overall solid fraction of the dispersed phase. This is a strong limitation of the model towards denser regimes.

When  $Pe$  increases, convective effects increase and the fluid transports more chemical species to the system at a constant consumption rate by the particles. This enhances the uniformity of the concentration field around particles, that tends to be equal to the inlet concentration at infinite flow rate, i.e.  $Pe \rightarrow \infty$ . This observation has been confirmed by analyzing statistics of the distribution of cup mixing concentration for different solid volume fractions and different Peclet numbers. However, moving to very high Peclet numbers (very often because of large values of the Schmidt number in liquids, see for example (Bale et al., 2019) where the effect of Schmidt number was investigated on transfer in packed beds) would yield stronger constraints on the numerical spatial resolution of the thin boundary layers and wakes around particles. The number of points per particle diameter becomes very soon prohibitive for direct numerical simulations as it scales with  $Pe^{1/3}$ .

Future work aims at addressing the extension of the established model to more complicated reaction kinetics (higher order) and reversible chemical reactions or multi species and multi reactions systems. This will involve finding the analytical solutions of concentration profiles within the catalyst particles in order to perform the internal external coupling. This will give information on enhancing the prediction of performances for realistic fixed or fluidized bed catalytic reactors. The current model is also to be coupled to heat transfer (Lu et al., 2019) to account for temperature

effect on reaction rate (exothermic reactions) and fluid density variations leading to natural convection effects. The current work represents a first step towards a general model for the 'reactive' Sherwood number in dense particulate flow systems with a first order chemical reaction. Upcoming efforts in terms of theoretical modeling can include axial dispersion of the reactants and products along the bed. Upcoming work also necessitates performing a multi scale micro meso comparison to test the performance of the model as a closure law for meso scale systems.

## Declaration of Competing Interest

The authors declare that they have no known competing financial interests or personal relationships that could have appeared to influence the work reported in this paper.

## Acknowledgments

This work was granted access by GENCI to the HPC resources of CINES under the allocations 2016 c20132b6699 and 2017 c20142b6699. This study is part of the ANR collaborative project More4Less (IFP EN, CORIA, IMFT and UBC).

## Appendix A

Figs. A.1 A.3.

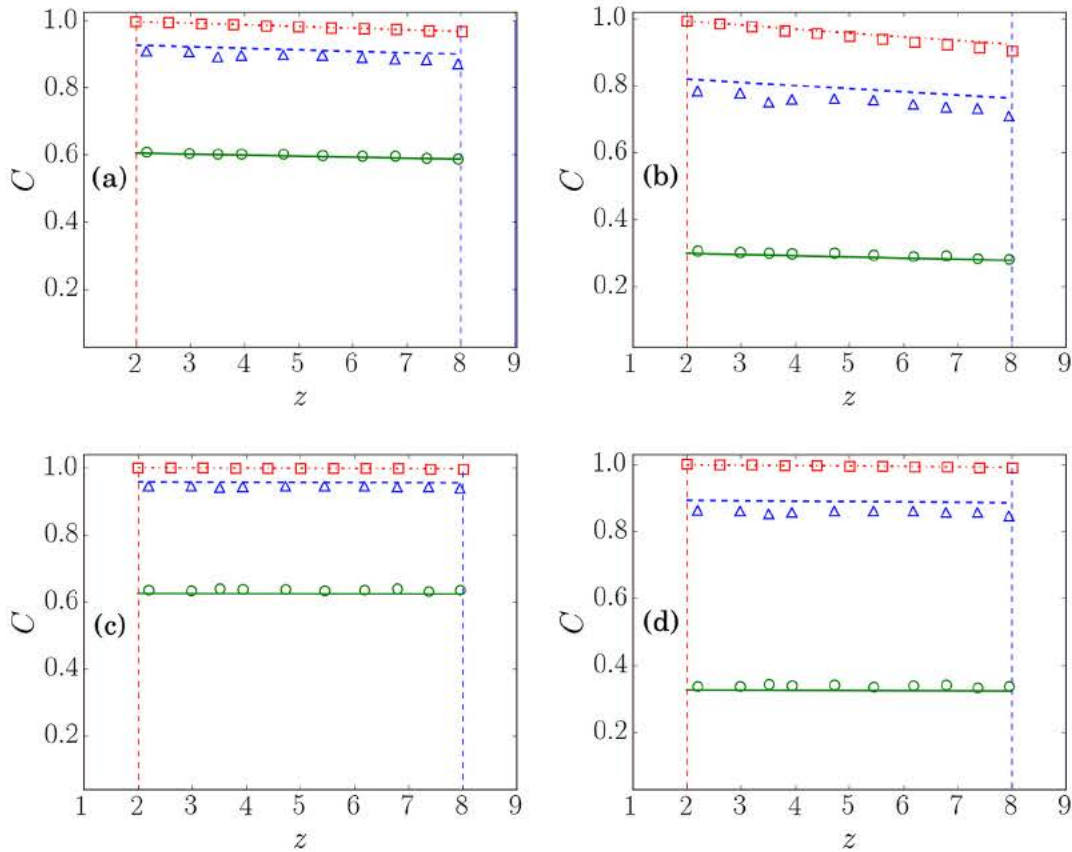


**Fig. A1.** Comparison of model prediction to numerical simulation results for  $\alpha_s = 0.1$ ,  $Re = 50$ , and  $\gamma = 0.1$ . Red color corresponds to  $\bar{C}(z)$ , blue color corresponds to  $\bar{C}_s(z)$  and green color corresponds to  $\bar{C}_v(z)$ . Lines stand for model and symbols for simulations. (a) and (b) correspond to  $Sc = 1$ , (c) and (d) correspond to  $Sc = 10$ , (a) and (c) correspond to  $Da = 40$  and (b) and (d) correspond to  $Da = 200$ . (For interpretation of the references to color in this figure legend, the reader is referred to the web version of this article.)

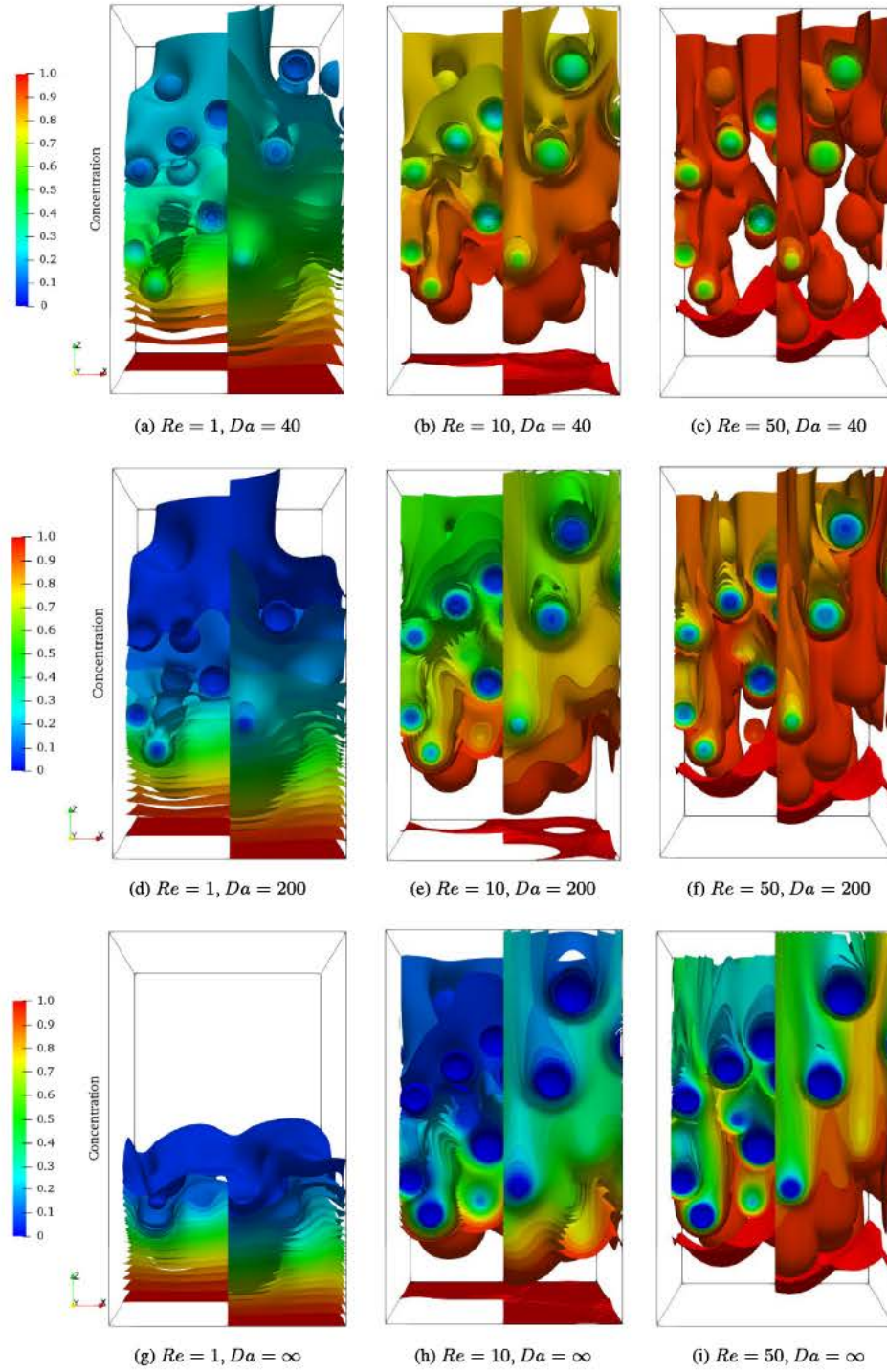


**Fig. A2.** Visualization of the interplay between convection, diffusion, and chemical reaction. Concentration isosurfaces for  $Sc = 1, \gamma = 0.1$  and  $\alpha_s = 0.1$ . From left to right, convection increases. From top to bottom, reaction rate increases. Along the diagonal from left-top to right-bottom both convection and reaction rate increase.

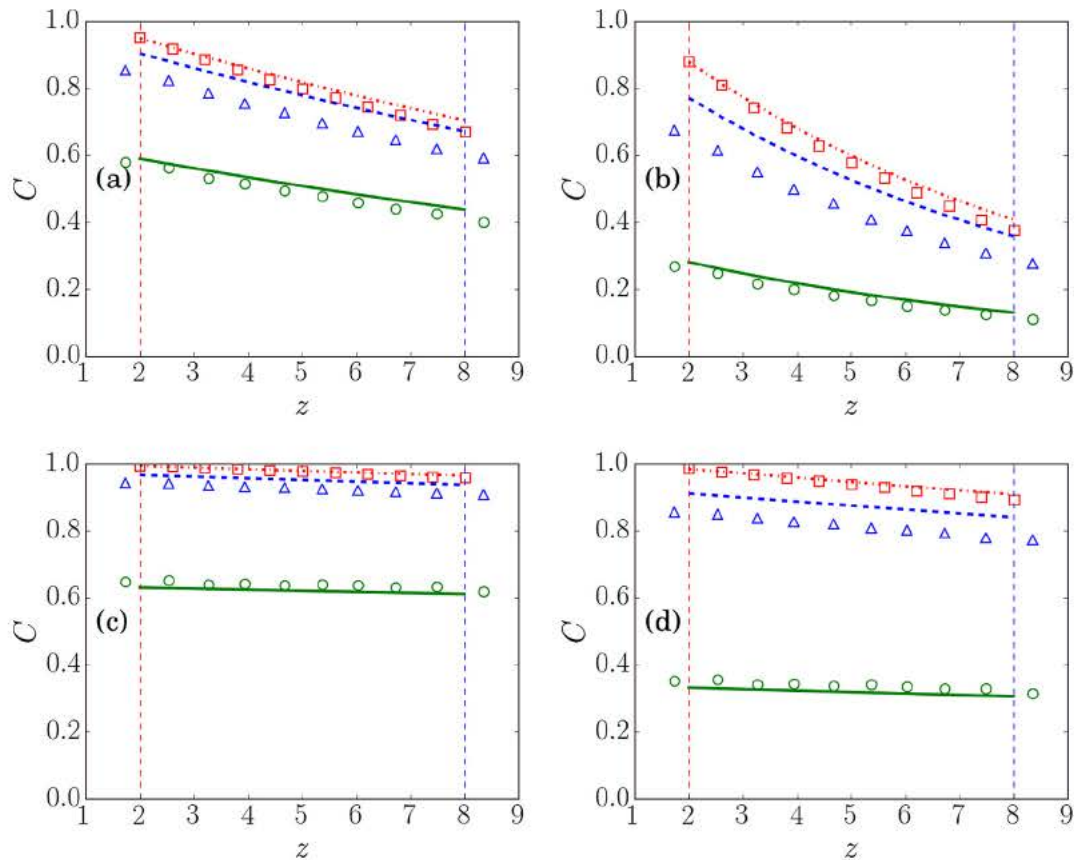


**Fig. A3.** Comparison of model prediction to numerical simulation results for  $\alpha_s = 0.5$ ,  $Re = 25$ , and  $\gamma = 0.1$ . Red color corresponds to  $\bar{C}(z)$ , blue color corresponds to  $\tilde{C}_s(z)$  and green color corresponds to  $\tilde{C}_p(z)$ . Lines stand for model and symbols for simulations. (a) and (b) correspond to  $Sc = 1$ , (c) and (d) correspond to  $Sc = 10$ , (a) and (c) correspond to  $Da = 40$  and (b) and (d) correspond to  $Da = 200$ . (For interpretation of the references to color in this figure legend, the reader is referred to the web version of this article.)

## References

- Bale, S., Sathe, M., Ayeni, O., Berrouk, A.S., Joshi, J., Nandakumar, K., 2017. Spatially resolved mass transfer coefficient for moderate reynolds number flows in packed beds: Wall effects. *Int. J. Heat Mass Transf.* 110, 406–415.
- Bale, S., Tiwari, S., Sathe, M., Berrouk, A.S., Nandakumar, K., Joshi, J., 2018. Direct numerical simulation study of end effects and d/d ratio on mass transfer in packed beds. *Int. J. Heat Mass Transf.* 127, 234–244.
- Bale, S., Tiwari, S.S., Nandakumar, K., Joshi, J.B., 2019. Effect of schmidt number and d/d ratio on mass transfer through gas-solid and liquid-solid packed beds: Direct numerical simulations. *Powder Technol.*
- Baxter, L.L., 1993. Ash deposition during biomass and coal combustion: a mechanistic approach. *Biomass Bioenergy* 4, 85–102.
- Bohn, C., Scott, S.A., Dennis, J.S., Müller, C., 2012. Validation of a lattice Boltzmann model for gas-solid reactions with experiments. *J. Comput. Phys.* 231, 5334–5350.
- Bridgwater, A., 1995. The technical and economic feasibility of biomass gasification for power generation. *Fuel* 74, 631–653.
- Dan, C., Wachs, A., 2010. Direct numerical simulation of particulate flow with heat transfer. *Int. J. Heat Fluid Flow* 31, 1050–1057.
- Deen, N.G., Peters, E., Padding, J.T., Kuipers, J., 2014. Review of direct numerical simulation of fluid-particle mass, momentum and heat transfer in dense gas-solid flows. *Chem. Eng. Sci.* 116, 710–724.
- Derksen, J., 2014. Simulations of solid-liquid mass transfer in fixed and fluidized beds. *Chem. Eng. J.* 255, 233–244.
- Dorai, F., Moura Teixeira, C., Rolland, M., Climent, E., Marcoux, M., Wachs, A., 2015. Fully resolved simulations of the flow through a packed bed of cylinders: Effect of size distribution. *Chem. Eng. Sci.* 129, 180–192.
- Fedkiw, R.P., Aslam, T., Merriman, B., Osher, S., 1999. A non-oscillatory eulerian approach to interfaces in multimaterial flows (the ghost fluid method). *J. Comput. Phys.* 152, 457–492.
- Feng, Z.G., Michaelides, E.E., 2000. A numerical study on the transient heat transfer from a sphere at high reynolds and peclét numbers. *Int. J. Heat Mass Transf.* 43, 219–229.
- Gao, J., Hou, Z., Guo, J., Zhu, Y., Zheng, X., 2008. Catalytic conversion of methane and co2 to synthesis gas over a la2o3-modified sio2 supported ni catalyst in fluidized-bed reactor. *Catal. Today* 131, 278–284.
- Glowinski, R., Pan, T., Hesla, T., Joseph, D., Periaux, J., 2001. A fictitious domain approach to the direct numerical simulation of incompressible viscous flow past moving rigid bodies: application to particulate flow. *J. Comput. Phys.* 169, 363–426.
- Glowinski, R., Pan, T.W., Hesla, T.I., Joseph, D.D., 1999. A distributed lagrange multiplier/fictitious domain method for particulate flows. *Int. J. Multiph. Flow* 25, 755–794.
- Gunn, D., 1978. Transfer of heat or mass to particles in fixed and fluidised beds. *Int. J. Heat Mass Transf.* 21, 467–476.
- van der Hoef, M.A., van Sint Annaland, M., Kuipers, J., 2004. Computational fluid dynamics for dense gas-solid fluidized beds: a multi-scale modeling strategy. *Chem. Eng. Sci.* 59, 5157–5165.
- Liu, X.D., Fedkiw, R.P., Kang, M., 2000. A boundary condition capturing method for poisson's equation on irregular domains. *J. Comput. Phys.* 160, 151–178.
- Lu, J., Das, S., Peters, E., Kuipers, J., 2018. Direct numerical simulation of fluid flow and mass transfer in dense fluid-particle systems with surface reactions. *Chem. Eng. Sci.* 176, 1–18.
- Lu, J., Peters, E., Kuipers, J., 2019. Direct numerical simulation of fluid flow and dependently coupled heat and mass transfer in fluid-particle systems. *Chem. Eng. Sci.*
- Rahmani, M., Wachs, A., 2014. Free falling and rising of spherical and angular particles. *Phys. Fluids* 26, 083301.
- Shao, X., Shi, Y., Yu, Z., 2012. Combination of the fictitious domain method and the sharp interface method for direct numerical simulation of particulate flows with heat transfer. *Int. J. Heat Mass Transf.* 55, 6775–6785.
- Shi, Y., Yu, Z., Shao, X., 2011. Combination of the direct-forcing fictitious domain method and the sharp interface method for the three-dimensional dielectrophoresis of particles. *Powder Technol.* 210, 52–59.
- Sulaiman, M., Climent, E., Hammouti, A., Wachs, A., 2019a. Mass transfer towards a reactive particle in a fluid flow: Numerical simulations and modeling. *Chem. Eng. Sci.* 199, 496–507.
- Sulaiman, M., Hammouti, A., Climent, E., Wachs, A., 2019b. Coupling the fictitious domain and sharp interface methods for the simulation of convective mass transfer around reactive particles: Towards a reactive sherwood number correlation for dilute systems. *Chem. Eng. Sci.* 198, 334–351.
- Sun, B., Tenneti, S., Subramaniam, S., 2015. Modeling average gas-solid heat transfer using particle-resolved direct numerical simulation. *Int. J. Heat Mass Transf.* 86, 898–913.
- Sun, B., Tenneti, S., Subramaniam, S., Koch, D.L., 2016. Pseudo-turbulent heat flux and average gas-phase conduction during gas-solid heat transfer: flow past random fixed particle assemblies. *J. Fluid Mech.* 798, 299–349.

- Tavassoli, H., Kriebitzsch, S., Van der Hoef, M., Peters, E., Kuipers, J., 2013. Direct numerical simulation of particulate flow with heat transfer. *Int. J. Multiph. Flow* 57, 29–37.
- Turn, S., Kinoshita, C., Zhang, Z., Ishimura, D., Zhou, J., 1998. An experimental investigation of hydrogen production from biomass gasification. *Int. J. Hydrogen Energy* 23, 641–648.
- Uhlmann, M., 2005. An immersed boundary method with direct forcing for the simulation of particulate flows. *J. Comput. Phys.* 209, 448–476.
- Wachs, A., 2011. Rising of 3d catalyst particles in a natural convection dominated flow by a parallel dns method. *Comput. Chem. Eng.* 35, 2169–2185.
- Wachs, A., Hammouti, A., Vinay, G., Rahmani, M., 2015. Accuracy of finite volume/ staggered grid distributed lagrange multiplier/fictitious domain simulations of particulate flows. *Comput. Fluids* 115, 154–172.
- Wehinger, G.D., Eppinger, T., Kraume, M., 2015. Detailed numerical simulations of catalytic fixed-bed reactors: Heterogeneous dry reforming of methane. *Chem. Eng. Sci.* 122, 197–209.
- Xia, J., Luo, K., Fan, J., 2014. A ghost-cell based high-order immersed boundary method for inter-phase heat transfer simulation. *Int. J. Heat Mass Transf.* 75, 302–312.
- Yu, Z., Shao, X., Wachs, A., 2006. A fictitious domain method for particulate flows with heat transfer. *J. Comput. Phys.* 217, 424–452.
- Zhang, B., Zhong, Z., Zhang, J., Ruan, R., 2018. Catalytic fast co-pyrolysis of biomass and fusel alcohol to enhance aromatic hydrocarbon production over zsm-5 catalyst in a fluidized bed reactor. *J. Anal. Appl. Pyrol.* 133, 147–153.